Generation and Characterization of Ultrashort DUV Pulses

Erzeugung und Charakterisierung ultrakurzer DUV Pulse

Corinna Melanie Konrad

München 2022

Generation and Characterization of Ultrashort DUV Pulses

Erzeugung und Charakterisierung ultrakurzer DUV Pulse

Corinna Melanie Konrad

Masterarbeit
an der Fakultät für Physik
der Ludwig–Maximilians–Universität
München

vorgelegt von
Corinna Melanie Konrad
aus Stuttgart

München, den 23. März 2022

Betreuer: Prof. Dr. Ferenc Krausz
Projektleiter: Dr. Johannes Schötz

Contents

List of Figures

List of Abbreviations

AOM	acusto-optical modulator
ATI	above threshold ionization
BBO	beta-barium borate
CEP	carrier envelope phase
CPA	chirped pulse amplification
CW	continuous wave
DFG	difference frequency generation
DUV	deep ultraviolet
FWHM	full width at half maximum
GNLSE	generalized nonlinear Schrödinger equation
GDD	group delay dispersion
GVD	group velocity dispersion
HCF	hollow core fiber
HHG	high harmonic generation
IR	infrared
LOPT	lowest order perturbation theory
MPI	multiphoton ionization
NIR	near infrared
NPS	nonlinear photoconductive sampling
Nd:YLF	neodymium-doped ytterbium lithium fluoride
Nd:YVO_4	neodymium yttrium vanadate
PFM	perforated mirror
PPLN	periodically-poled lithium-niobate
RDW	resonant dispersive wave
SFA	strong-field approximation
SPM	self-phase modulation
TIPTOE	tunneling ionization with a perturbation for the time-domain observation of an electric field
Ti:Sapph	Ti:Sapphire
UV	ultraviolet
VIS	visible
VUV	vacuum ultraviolet

Abstract

The study of ultrafast electronic dynamics on the attosecond timescale with optical laser pulses requires field-resolved measurements for the investigation and ultimately the control of the light-matter interactions. Additionally, the investigation of these dynamics in large band gap materials greatly benefits from the availability of highly energetic photons for the linear excitation of the electrons from the valence into the conduction band.
The first part of this work studies the generation of high energetic photons by extending the spectrum of a pulsed laser reaching from the visible to the near-infrared into the ultraviolet via nonlinear optical processes, predominantly self-phase modulation, taking place in an argon-filled hollow core fiber. The extension of the spectrum down to approximately $\lambda =$ 170 nm corresponding to a photon energy of approximately 7 eV is recorded. The aim is to further increase the energy conversion efficiency of the ultraviolet spectral components. Moreover, increasing the bandwidth of the spectrum to an ultrabroadband continuum opens the possibility of temporally compressing the pulses further as predicted from the minimum time-bandwidth product.
The second part of the thesis focuses on the usage of the two field-resolved measurement techniques tunneling ionization with a perturbation for the time-domain observation of an electric field (TIPTOE) [1] and nonlinear photoconductive sampling (NPS) [2] for the recording of the generated pulses. Both techniques record the spectrum of the original pulse and NPS additionally shows the extension of the spectrum down to $\lambda = 300$ nm. Below this wavelength both measurements are dominated by an artifact. The origin and approaches to mitigate this artifact are discussed. The goal for the future is the elimination of the artifact and the extension of the measurement techniques across the deep ultraviolet region down to the measured wavelength cutoff at approximately 170 nm.

Chapter 1

Introduction

Since the development of the first laser in 1960 by Maiman [3] lasers have been one of the most important tools in experimental physics as they are a highly coherent light source. Pulsed lasers became available in the same decade producing lightpulses in the nanosecond [4] and picosecond [5] range. Pulsed lasers can be used in so called pump-probe experiments for the time-resolved measurement of physical properties. Here, the pump pulse excites a medium via absorption of photons. The state of the system is then probed with another time delayed pulse. Variation of the time delay scans the evolution of the system following the excitation introduced by the pump pulse.
Today Ti:Sapphire lasers [6], invented in the 1980s, are the most prominent source of ultrashort pulses. They are able to produce pulses in the femtosecond range that enable time-resolved measurements of chemical reactions. For example, the rearrangement of atoms is a process that takes place in the femtosecond range[7]. Using extremely nonlinear, non-perturbative processes like tunneling emission of an electron in a strong electric field can confine the light-matter interaction to a fraction of a half-cycle oscillation of a laser pulse and therefore opens the possibility of pushing the time-resolution to the attosecond timescale. Being able to measure and control processes at the attosecond timescale provides the possibility to study the motion of electrons in atoms and molecules as well as processes in future lightwave-driven electronics.
In order to control electronic processes on sub-cycle timescales field-resolved pulse characterization techniques are required. In recent years, nonlinear photoconductive sampling (NPS) [2] and tunneling ionization with a perturbation for the time-domain observation of an electric field (TIPTOE) [1] have been introduced. NPS is an extension of terahertz (THz) photoconductive sampling. Free carriers are created in a nonlinear photoexcitation by the pump pulse and displaced by the signal pulse. The nonlinearity of the photoexcitation creates a sub-cycle gate. The bandwidth of this technique should in theory only be limited by the photoexcitation time. Former publications demonstrated the technique down to $\lambda = 275$ nm in the UV spectral range, limited by the bandwidth of the laser pulses used in the experiments. The aim of this thesis is to extend the bandwidth of the NPS technique, covering the deep ultraviolet (DUV) and extending to the vacuum ultraviolet (VUV).

TIPTOE is a measurement technique relying on the perturbation of a strong-field process by a weak probe field. If the probe field is weak enough, the Taylor expansion can be applied. In this case the change of the strong-field observable, which is the ionization yield in TIPTOE, is proportional to the perturbing probe field.
An advantage of NPS and TIPTOE compared to other field-resolved techniques is the rather simple setup for the measurements. They both rely on a current measurement conducted with a pair of electrodes and read out by a lock-in amplifier.
In order to test the bandwidth limitations of the field sampling techniques, ultrabroadband continuum generation is another goal of this thesis. This is realized via nonlinear broadening in a gas-filled hollow core fiber (HCF). Reaching wavelengths of approximately 170 nm and therefore higher energetic photons in the range of up to 7 eV can be used to study ultrafast electronic dynamics in small as well as in large band gap materials. The high photon energy allows for a linear excitation from the valence band into the conduction band in a number of different materials. The band gap of several materials is shown in Fig. 1.1. The band gaps of several oxides and halides are in the region that is planned to be covered with the broadened spectrum and could be excited directly with the generated UV-pulses.
Moreover, temporal compression of the ultrabroadband pulses up to the limit introduced by the time-bandwidth product will result in the generation of pulses shorter than the original pulses from the FP3-beamline due to the larger spectral bandwidth.

The thesis is organized in the following way. Chapter 2 introduces the theoretical foundations that are necessary to understand this work. It offers a brief overview over the description of ultrashort pulses, nonlinear optical phenomena and strong-field ionization. Chapter 3 introduces the laser and the experimental setup that has been built during the course of this thesis for the experiments conducted in it. Moreover, the two field-resolved sampling techniques are explained further in this chapter. Chapter 4 presents the results of the supercontinuum generation down to the VUV while chapter 5 demonstrates the measurements of field-resolved pulses. The experimental results of the supercontinuum generation are compared to simulation results in the respective chapter.

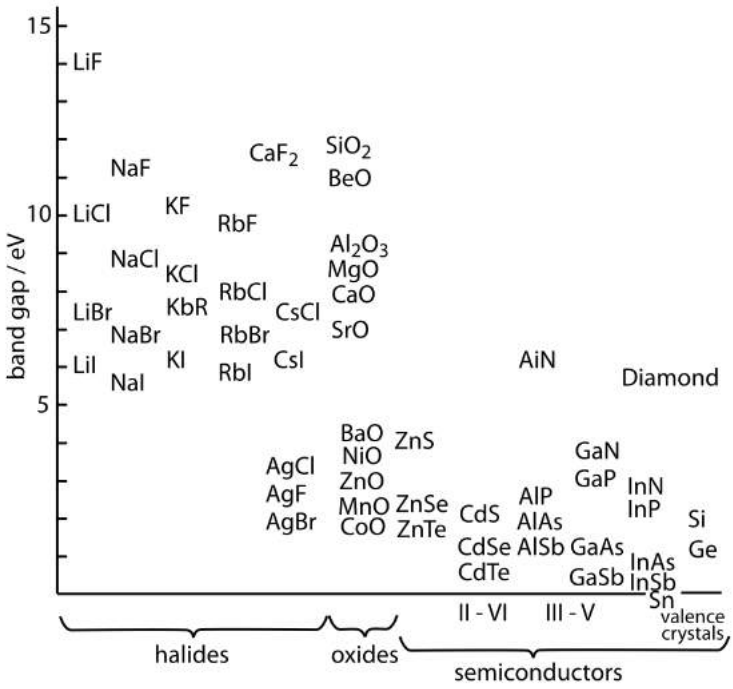

Figure 1.1: Band gaps of different materials. For linear excitation of electrons, photons with at least the same energy of the band gap have to be used. The aim of the experiments in this thesis is to reach photon energies of up to 7 eV. Reprinted by permission from Springer Nature Customer Service Centre GmbH: Springer Nature, Bands and Band Gaps in Solids by Karl W. Böer ©2013 [8].

Chapter 2

Theoretical Background

This chapter provides the theoretical background of attosecond physics for the understanding of the detection process. Additionally, the topic of nonlinear optical phenomena for the understanding of the deep UV generation process is discussed. It starts with a brief overview of the mathematical description of ultrashort pulses and their characteristics. Secondly, nonlinear optical phenomena arising from the interaction of high intensity laser pulses with nonlinear media are covered. Furthermore, different processes of strong-field ionization and the three-step model describing the propagation of an electron ionized from a bound state into the continuum are explained in this chapter.

2.1 Ultrashort Pulses

The derivation for the electric field representation of an ultrashort pulse follows [9]. Furthermore the description of the spectral phase and the characterization of the pulse is related to [10].

Electromagnetic waves are described by an electric field and a magnetic field perpendicular to the electric field. The fields are related via Maxwell's equations. Therefore the magnetic field can be calculated when the electric field is known and it suffices to describe an electromagnetic wave with the electric field only. The electric field of a laser pulse can be described equivalently both in the time- and the frequency-domain. The two descriptions are related via the Fourier transform as follows

$$\tilde{E}(\omega) = \int_{-\infty}^{\infty} E(t)\, e^{-i\omega t} \mathrm{d}t \tag{2.1}$$

$$E(t) = \frac{1}{2\pi} \int_{-\infty}^{\infty} \tilde{E}(\omega)\, e^{i\omega t} \mathrm{d}\omega. \tag{2.2}$$

In this case $E(t)$ is the real electric field and $\tilde{E}(\omega)$ is the complex spectrum of the field strength. Often the electric field is separated into two complex functions by separating the spectrum into the positive frequencies on one hand and the negative frequencies on the other hand

$$E\left(t\right) = \tilde{E}^{+}\left(t\right) + \tilde{E}^{-}\left(t\right) \tag{2.3}$$

$$\tilde{E}\left(\omega\right) = \tilde{E}^{+}\left(\omega\right) + \tilde{E}^{-}\left(\omega\right). \tag{2.4}$$

$\tilde{E}^{+}\left(\omega\right)$ is a function that is equal to $\tilde{E}\left(\omega\right)$ for positive frequency components ω and 0 for the negative frequency components while $\tilde{E}^{-}\left(\omega\right)$ contains the negative frequency components and is therefore 0 where $\omega > 0$ and equal to $\tilde{E}\left(\omega\right)$ for $\omega < 0$.
Usually to describe the electric field of an electromagnetic wave, in our case of an ultrashort pulse, the complex electric field component $\tilde{E}^{+}\left(t\right)$ is used. This function can be calculated from the spectrum via

$$\tilde{E}^{+}\left(t\right) = \frac{1}{2\pi}\int_{0}^{\infty}\tilde{E}\left(\omega\right)e^{i\omega t}\mathrm{d}\omega = \frac{1}{2\pi}\int_{-\infty}^{\infty}\tilde{E}^{+}\left(\omega\right)e^{i\omega t}\mathrm{d}\omega. \tag{2.5}$$

This complex function can also be expressed as

$$\tilde{E}^{+}(t) = A(t)e^{i(\phi_0+\phi(t)+\omega_0 t)}, \tag{2.6}$$

where $A(t)$ is the envelope that can usually be described as a Gaussian

$$A(t) = \exp\left(-2\ln\left(2\right)\left(t/\tau_{\mathrm{FWHM}}\right)^{2}\right), \tag{2.7}$$

with τ_{FWHM} being the full width at half maximum (FWHM) of the intensity. ω_0 is the carrier frequency that describes the rapidly varying component of the field. ϕ_0 is the carrier-envelope phase (CEP) that describes the relative phase between the oscillating field and the envelope which will be discussed further in the next section. The second phase term $\phi(t)$ is necessary for defining the instantaneous frequency ω_{inst} as

$$\omega_{\mathrm{inst}} = \omega_0 + \frac{\mathrm{d}}{\mathrm{d}t}\phi(t). \tag{2.8}$$

Equivalently in the frequency domain the spectrum for the positive frequencies can be represented as

$$\tilde{E}^{+}\left(\omega\right) = \sqrt{S\left(\omega\right)}e^{i\psi(\omega)}, \tag{2.9}$$

where $S(\omega)$ is the spectral intensity that acts as the envelope and $\psi(\omega)$ the spectral phase that is the argument of an oscillating complex function. The spectral phase is a measurement for the duration of a pulse. Therefore, it is important to have control over it. Keeping a flat spectral phase is one of the most challenging aspects in working with a laser. The spectral intensity envelope can again be described with a Gaussian and the envelopes in the different domains are related via the time-bandwidth product. This is a property following

from the Fourier transformation and it gives a connection between the FWHM in the time and the frequency domain. The minimum time-bandwidth product for Gaussian-shaped pulses is

$$\tau_{\mathrm{FWHM}} \cdot \Delta\omega = 0.441 \cdot 2\pi. \tag{2.10}$$

This is only reached for bandwidth-limited pulses with a flat phase. How close a pulses time-bandwidth product is to the minimal value is often used as a measure of the pulse quality.
The spectral phase in the expression of the electric field can be expanded into a Taylor series around the carrier frequency as

$$\psi(\omega) = \sum_{j=0}^{\infty} \frac{\psi^{(j)}(\omega_0)}{j!} (\omega - \omega_0)^j . \tag{2.11}$$

The zeroth order term in this sum describes the CEP. The first order term describes the group delay of the pulse which is the temporal delay of the pulse envelope. The second order term is responsible for the group delay dispersion (GDD). This will be discussed further in the next chapter.

2.1.1 Carrier-envelope phase (CEP)

The CEP is defined as the phase difference between the carrier wave and the peak of the pulse envelope. The CEP is a particularly important feature in the realm of attosecond physics and few-cycle pulses as there is a strong dependence of the electric field on the CEP whereas it can be neglected for longer pulses. This is illustrated in Fig. 2.1.
The CEP is a helpful tool for finding and measuring processes that depend on the field of a pulse as for example strong-field tunneling that will be discussed later rather than its intensity envelope which also opens the possibility of measuring the CEP with these processes in turn. Furthermore, precise control over the CEP leads to attosecond precision in the control over processes happening on a sub-cycle timescale and opens the possibility to separate the contributions of the individual half-cycles.

2.1.2 Dispersion

Dispersion describes the phenomenon that the refractive index of a material is frequency dependent. It always occurs when an electromagnetic wave propagates through a medium. To look at this phenomenon mathematically the frequency domain is used. The wavevector β can be used in this description instead of the spectral phase. The description for an electric field after a propagation distance L in a medium is given by

$$E(t, L) = \int \tilde{E}(\omega)\, e^{i\omega t + i\psi_0(\omega) - i\beta(\omega)L}. \tag{2.12}$$

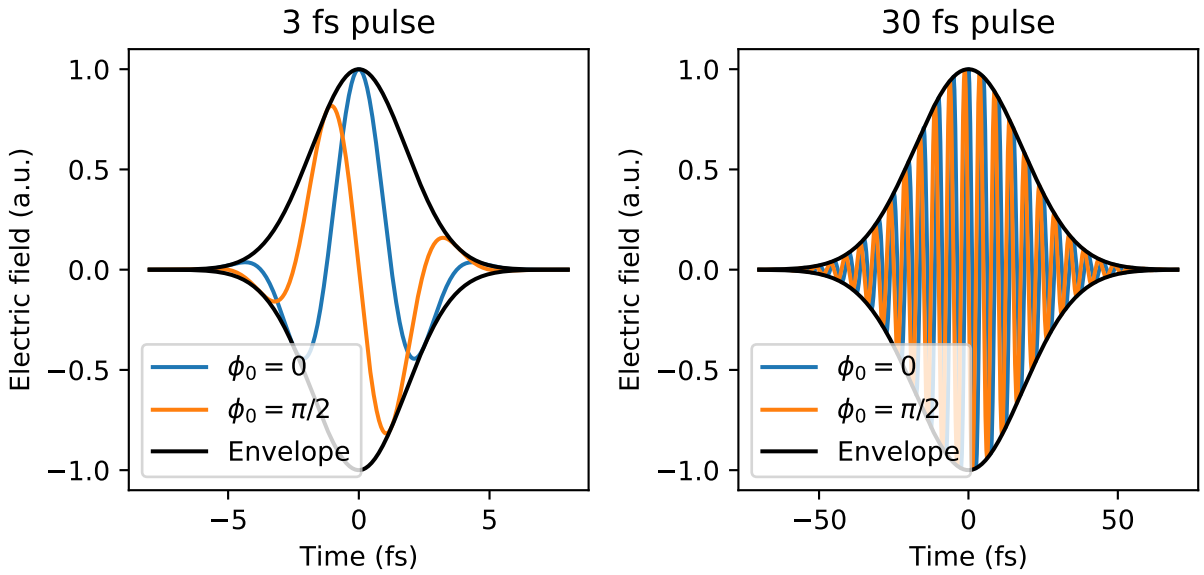

Figure 2.1: Illustration of the dependence of the electric field on the CEP. **(a)** 3 fs few-cycle pulse. The peak amplitude strongly varies with the value of the CEP. **(b)** 30 fs pulse with the same carrier frequency. The CEP dependence of the amplitude is neglectable.

The relationship between the spectral phase and the wavevector β is therefore $\psi(\omega) = \psi_0(\omega) - \beta(\omega)L$ with L being the propagation distance. As well as the spectral phase the wavevector can also be approximated as a Taylor series in the following manner

$$\beta(\omega) = \sum_{j=0}^{\infty} \frac{\beta_j}{j!} (\omega - \omega_0)^j \tag{2.13}$$

with the beta coefficients

$$\beta_j = \frac{\mathrm{d}^j}{\mathrm{d}\omega^j} \beta(\omega) . \tag{2.14}$$

As mentioned above the zeroth order term describes the phase velocity whereas the first order term is a measurement of the group velocity. The second order term describes the group velocity dispersion (GVD). If this value is different from 0 the group velocity is frequency dependent which is a result of the dispersion relation which describes the refractive index of a material as a frequency dependent quantity. As a consequence, a pulse that is originally compressed to its Fourier-limit, gets chirped and elongated as it propagates through the material.
Depending on the function of the refractive index and therefore also the sign of β_2 there are two different kinds of chirp.
In the regime of normal dispersion the refractive index increases with frequency and therefore the red components of the light are faster and move to the leading edge of the pulse

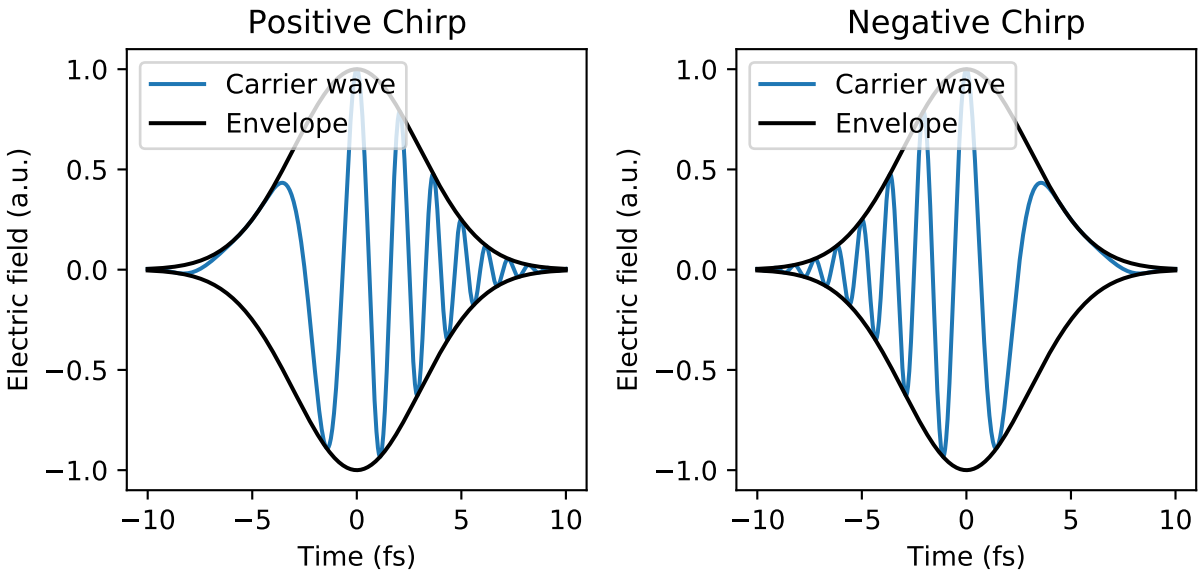

Figure 2.2: Dispersion of the different frequencies in a pulse. **(a)** Normal dispersion regime. The lower frequencies are in the leading edge of the pulse. **(b)** Anomalous dispersion regime. The shorter wavelengths are in the leading edge of the pulse.

whereas the blue frequencies are in the trailing edge. This is called a positive chirp and it occurs for $\beta_2 > 0$.
The regime of anomalous dispersion where $\beta_2 < 0$ holds, is characterized by a decreasing refractive index with increasing frequency. In contrast to the normal dispersion regime the blue frequency components are faster in this region and therefore move to the leading edge of the pulse introducing a negatively chirped pulse. Pulses with negative and positive chirp are displayed in Fig. 2.2.
Dispersion of any kind leads to an elongation of the pulse due to the different speeds of the frequency components.
Different resonances in materials introduce the phenomenon that there is a normal dispersion regime as well as an anomalous dispersion regime. Below a resonance wavelength occurs positive GVD and above the resonance frequency occurs negative GVD. In the regime between the resonances there is the so-called zero dispersion wavelength λ_{zd} where $\beta_2 = 0$ and only higher order dispersion plays a role. This phenomenon is important for example in the case of hollow core fibers as used in this thesis.

2.2 Nonlinear optical phenomena

The propagation of a laser pulse in a medium is described by Maxwell's equations. In the case of a charge- and current-free ($\rho = 0$ and $\vec{J} = \mathbf{0}$) environment they are

$$\nabla \cdot \vec{D} = 0 \tag{2.15}$$

$$\nabla \cdot \vec{B} = 0 \tag{2.16}$$

$$\nabla \times \vec{E} = -\frac{\partial \vec{B}}{\partial t} \tag{2.17}$$

$$\nabla \times \vec{H} = \frac{\partial \vec{D}}{\partial t}, \tag{2.18}$$

with the following relationships for the electric displacement field $\vec{D}$ and the magnetic field strength $\vec{H}$

$$\vec{D} = \epsilon_0 \vec{E} + \vec{P},\ \vec{B} = \mu_0 \vec{H}, \tag{2.19}$$

where ϵ_0 is the vacuum permittivity and μ_0 the vacuum permeability that are connected to the speed of light via $\epsilon_0 \mu_0 = 1/c^2$. The nonlinear wave equation can be obtained from these relations as

$$\left(\Delta - \frac{1}{c^2}\frac{\partial^2}{\partial t^2}\right) \vec{E}\left(\vec{r}, t\right) = \frac{1}{\epsilon_0 c^2}\frac{\partial^2}{\partial t^2}\vec{P}\left(\vec{r}, t\right). \tag{2.20}$$

$\Delta = \nabla^2 = \frac{\partial^2}{\partial x^2} + \frac{\partial^2}{\partial y^2} + \frac{\partial^2}{\partial z^2}$ is the Laplace operator. The polarization $\vec{P}$ on the right hand side of this equation is the response of the material. It can be divided into a linear and a nonlinear part

$$\vec{P} = \vec{P}_{\mathrm{L}} + \vec{P}_{\mathrm{NL}} = \epsilon_0 \left(\chi^{(1)}\vec{E} + \chi^{(2)}\vec{E}^2 + \chi^{(3)}\vec{E}^3 + ...\right), \tag{2.21}$$

where $\vec{P}_{\mathrm{L}} = \epsilon_0 \chi^{(1)} \vec{E}$ is the linear polarization and the other components are the nonlinear polarization components. $\chi^{(n)}$ is the n-th order susceptibility. The wave equation can be reduced to the propagation direction of the electro-magnetic wave and by Fourier transforming and using the relation $n^2(\omega) = 1 + \chi^{(1)}(\omega)$ for the complex refractive index $n(\omega)$ the wave equation in the frequency domain becomes

$$\left(\frac{\partial^2}{\partial z^2} + \frac{n^2(\omega)}{c^2}\omega^2\right) \tilde{E}\left(z, \omega\right) = -\omega^2 \mu_0 \tilde{P}\left(z, \omega\right). \tag{2.22}$$

The solution to the homogeneous equation, where $P_{\mathrm{NL}} = 0$ is a plane wave

$$E\left(z, t\right) = E_0\left(z, t\right) e^{i(\omega_0 t - k_0 z)} \tag{2.23}$$

with the wave vector

$$k_0 = \omega_0^2 n^2(\omega_0)/c^2. \tag{2.24}$$

From equations (2.22) to (2.24) it can be concluded that only the nonlinear polarization acts as a sourceterm and creates new frequency components.

2.2.1 Kerr effect

This and the following paragraphs are based on the explanations in [11] and [12].

It can be shown that second-order nonlinear processes can only take place in non-centrosymmetric crystals. Liquids, gases and amorphous like glass display inversion symmetry and therefore there is no contribution of second-order nonlinearities in these materials. Third-order nonlinear processes on the other hand occur independent of the inversion symmetry. For a laser pulse with an electric field strength on the order of the electric field of the atom $E_{\text{atom}} \approx 5.14 \cdot 10^{11}\text{V/m}$ corresponding to an intensity of $I_{\text{atom}} = 3.5 \cdot 10^{16}\text{W/cm}^2$ the nonlinear contributions of different orders are of the same order of magnitude. As the intensities used in the experiments in this thesis are smaller and therefore the higher-order contributions have a smaller impact on the total polarization, the strongest contribution in a gas with inversion symmetry is of the third order

$$P_{\text{NL}} = \epsilon_0 \chi^{(3)} E^3(t). \tag{2.25}$$

Assuming an incoming monochromatic wave of the form $E(t) = E_0 \cos(\omega t)$ and using a mathematical identity to avoid the $\cos^3(\omega t)$ term the polarization response of the material can be written as

$$P^{(3)}(t) = \frac{1}{4}\epsilon_0 \chi^{(3)} E_0^3 \cos(3\omega t) + \frac{3}{4}\epsilon_0 \chi^{(3)} E_0^3 \cos(\omega t). \tag{2.26}$$

The first term in this expression describes the third harmonic generation where a field of frequency ω generates a response at frequency 3ω.
The second term in the equation leads to a contribution to the polarization at the same frequency as the incident field and therefore alters the refractive index the electro-magnetic wave at the frequency ω experiences. The relationship between intensity and electric field allows to derive the proportionality $E_0^3 \cos(\omega t) \propto IE(t)$. Taking into account the linear polarization and using the Taylor approximation of the squareroot the refractive index can now be written as

$$n = n_0 + I n_2, \tag{2.27}$$

where n_0 is the linear refractive index and n_2 represents the nonlinear refractive index characterizing the strength of the optical nonlinearity of the third order via

$$n_2 = \frac{3}{2 n_0^2 \epsilon_0 c} \chi^{(3)}. \tag{2.28}$$

2.2.2 Self-phase modulation (SPM)

The refractive index is, as derived above, intensity dependent which means a pulse of light with a strongly varying intensity envelope will see a time-dependent refractive index leading to a time-dependent phase velocity. The leading edge of the pulse, where there is an increase in intensity, will also increase the refractive index which leads to a stretch of

the cycle of the electric field and this in turn leads to red shift. At the trailing edge of the pulse the refractive index decreases and leads to a blue shift. This is shown in Fig. 2.3. Mathematically this can be described in the following way. In a thin medium of length l a pulse experiences a phase shift of

$$\Delta\phi = 2\pi\frac{n(t)l}{\lambda}, \tag{2.29}$$

which leads to a nonlinear phase shift of

$$\Delta\phi_{\mathrm{NL}}(t) = 2\pi\frac{n_2 I(t)l}{\lambda}. \tag{2.30}$$

This in turn leads to a change in the instantaneous frequency of

$$\Delta\omega_{\mathrm{inst}} = \frac{\partial}{\partial t}\Delta\phi_{\mathrm{NL}}(t), \tag{2.31}$$

that is proportional to the time derivative of the intensity. In total the intensity dependent refractive index leads to the generation of new frequencies and therefore to the spectral broadening of the pulse. As the intensity envelope of the pulse is symmetric, the new frequencies are also added in a symmetric way to the spectrum. This broadening in the frequency domain can be used to compress the pulse further in the time domain.

2.2.3 Self-steepening

A change in the refractive index does not only lead to a phase shift but also to a change in the group velocity. In a region with higher refractive index the group velocity is slower than in a region with lower intensity. Therefore the peak of the pulse moves slower because the higher intensity leads to a higher refractive index. The edges of the pulse do not experience this strong shift in the refractive index and therefore move faster. This leads to the peak of the pulse moving to the trailing edge of the pulse. The intensity envelope of the pulse is then steepened in the trailing part of the pulse. If the pulse moves so far in the medium that the envelope becomes vertical, the pulse breaks up. This phenomenon is called optical shock. Furthermore the spectrum is affected by self-steepening. It takes place at the same time as SPM which produces a symmetric spectrum as was shown before. This spectrum becomes asymmetric due to the effect of self-steepening. To realize the steeper edge of the pulse, higher frequencies are necessary. Therefore the spectrum is extended into the higher frequency range. Because the spectral power in the red and the blue region has to stay the same this leads to a decrease of the peak spectral power in the high frequency region.

2.2.4 Self-focusing

The intensity dependence of the refractive index does not only have an influence due to the time varying intensity envelope but also the spatial intensity profile of the pulse must be

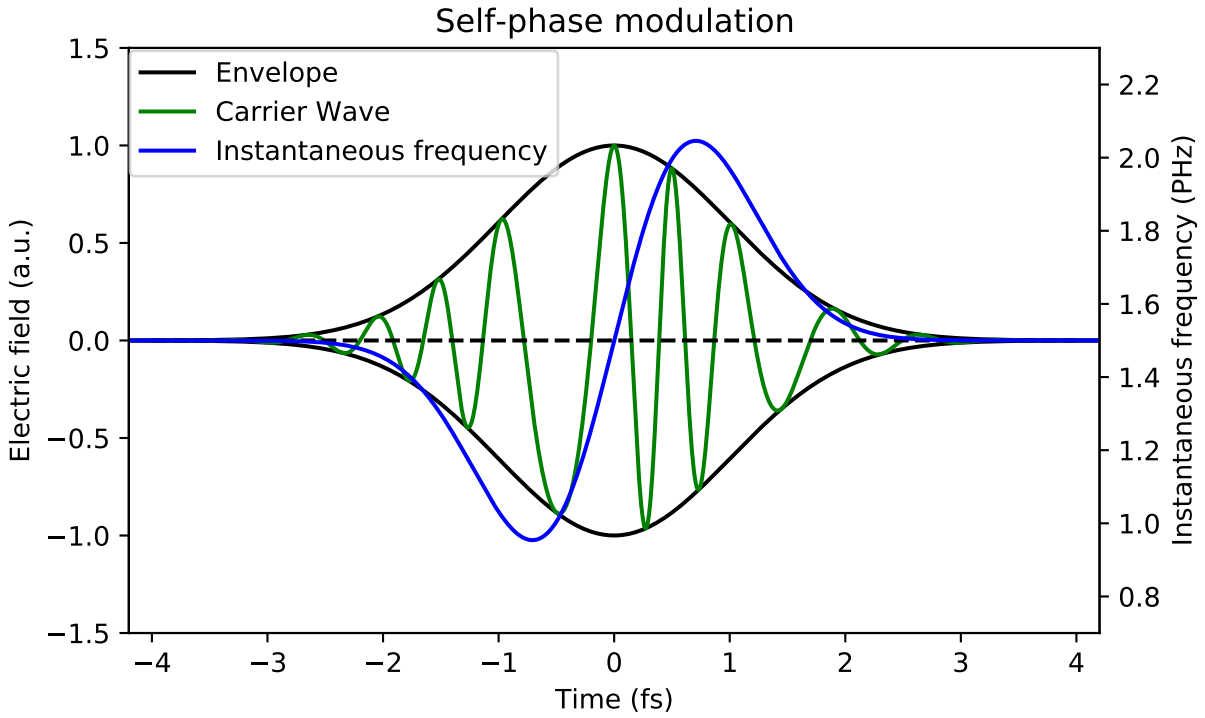

Figure 2.3: Time-domain representation of the self-phase modulation. The time-dependent intensity (proportional to the square of the electric field amplitude shown in black) causes a shift in the refractive index and therefore a change in the instantaneous frequency (blue). The phase of the carrier wave is modulated. The instantaneous frequency matches the carrier frequency at the peak of the electric field. There is a red shift in the leading edge of the pulse (on the left) and a blue shift in the trailing edge of the pulse.

considered. The refractive index has the highest value where the intensity is the strongest which is in the center of the beam. This leads to the material behaving in the same way a convex lens does and focusing the beam. This behavior is countered by the diffraction that increases with a more tightly focused beam. The beam is considered self-trapped when focusing and diffraction cancel each other out and the beam has a constant beam diameter. Self-focusing is the dominating process and leads to a collapse of the beam if the input power of the beam exceeds the critical power (here for a Gaussian beam)

$$P_{\mathrm{cr}} = \frac{3.77\lambda_0^2}{8\pi n_0 n_2}. \tag{2.32}$$

2.3 Strong-field Ionization

The measurement of the electric field of an electromagnetic laser pulse relies on the strong-field photoionization process of atoms and molecules where the photon energy is much smaller than the binding energy of the electron, but the field is strong enough that nonlinear ionization occurs nevertheless. The theoretical foundation for photoionization was delivered by Keldysh [13]. In his work, he introduces the Keldysh parameter γ to distinguish between the two limiting cases of multiphoton ionization in a weak electric field and the tunneling regime for strong electric fields

$$\gamma = \sqrt{\frac{I_p}{2U_p}}. \tag{2.33}$$

In this equation U_p is the cycle averaged kinetic energy of the oscillatory motion of a free electron of mass m_e and charge E in an oscillating electric field which is known as the ponderomotive potential. It is defined as

$$U_p = \frac{e^2 E_0^2}{4 m_e \omega^2} = 9.22 \text{ eV} \cdot I \left[10^{14} \text{ W/cm}^2\right] \cdot \lambda \left[\mu\text{m}\right]^2, \tag{2.34}$$

with E_0 and ω the peak amplitude and the central frequency of the oscillating electric field respectively.
For $\gamma \gg 1$ the ponderomotive energy is small compared to the binding energy and the emission of the electron is described as multiphoton ionization.
For $\gamma \ll 1$ the ponderomotive energy is large compared to the binding energy due to the strong electric field of the laser. The ionization in this regime is described by tunneling.
Keldysh's work was extended by Perelomov, Popov and Terentev [14, 15] with the calculation of an analytic expression for the ionization probability of atoms in an oscillating electric field.

2.3.1 Multiphoton ionization

Photoionization in the weak field regime, characterized by $\gamma \gg 1$, can be described in the perturbation theory. The atomic potential in this case is orders of magnitude stronger

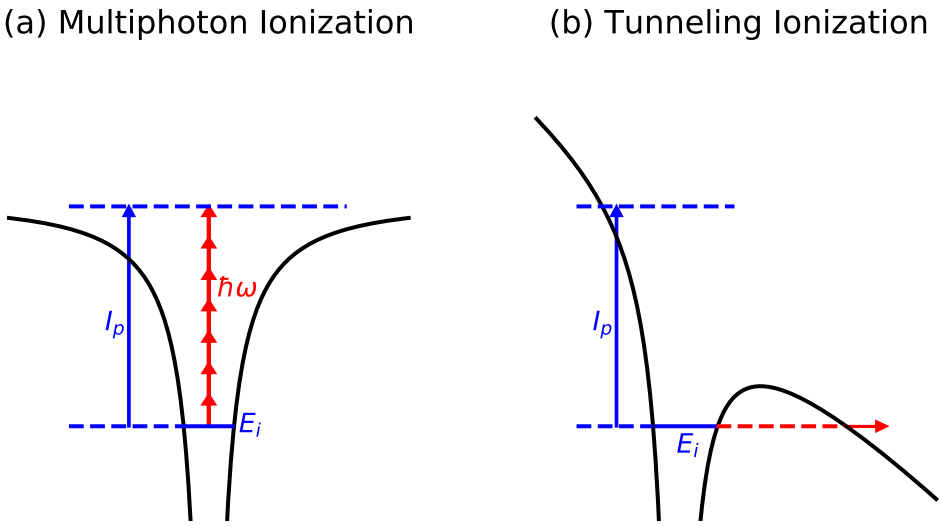

Figure 2.4: Schematic representation of strong field photoemission. **(a)** Multiphoton ionization. The energy of several photons (here: 7) is combined to lift the electron from the bound state in the atomic potential into the continuum. **(b)** Tunneling ionization. The electric field of the incoming laser is strong enough to alter the atomic potential. The barrier for the electron to get to the continuum gets smaller and the electron can tunnel out. The image is adapted from [16].

than the electric laser field. If the energy of a photon at the wavelength of the laser is smaller than the binding energy of an electron multiple photons can be accumulated for the photoemission. A schematic representation of the process is shown in Fig. 2.4 . This process is known as multiphoton ionization (MPI). The required number of photons is given by $n = \lceil I_\mathrm{p}/\hbar\omega \rceil$, where the excess energy that is not needed to ionize the ion is transferred to the electron as kinetic energy. The multiphoton ionization rate can be calculated in the lowest order perturbation theory (LOPT) [17] and its dependence on the intensity and therefore also the peak electric field can be described in a power law

$$w_\mathrm{MPI} = \sigma_\mathrm{n} I^n, \tag{2.35}$$

where σ_n is a generalized cross section and I is the laser intensity.
If the laser intensity increases and $\gamma \to 1$ more photons than the minimum number required for the ionization process are absorbed [17]. This process is called above threshold ionization (ATI) and it produces photoelectrons with the kinetic energies

$$E_\mathrm{kin} = (n + s)\,\omega - I_\mathrm{p} \tag{2.36}$$

with s the number of absorbed photons above the ionization threshold. Further increasing the field strength leads to effects like channel closing where the lowest peak in the photoelectron spectrum is suppressed [18].

2.3.2 Tunneling

Increasing the intensity of the laser leads to the perturbation theory no longer being valid. In this regime, where $\gamma \ll 1$, the electric field of the laser is in the same order of magnitude as the atomic potential which leads to a significant modulation of the atomic potential. This generates a potential barrier with a finite width depending on the field strength, which creates the possibility of an electron tunneling out as described by quantum mechanics. This is shown in Fig. 2.4. The tunneling ionization rate w_Tunnel is derived in the paper by Ammosov, Delone and Krainov [19] also known as the ADK-theory. In contrast to the process of multiphoton ionization the ionization rate in the tunneling regime is dependent on the electric field strength $E(t)$ exponentially instead of in a power law

$$w_\mathrm{Tunnel}(t) = \exp\left[-\frac{2}{3}\frac{(2I_p)^{3/2}}{E(t)}\right]. \tag{2.37}$$

This shows a strong dependence of the ionization rate on the electric field that is strongly dependent on the CEP in ultrashort laser pulse.

2.3.3 Three-step model

To understand how the electron propagates after the photoionization the three-step model (or simpleman's model) is considered. It becomes apparent that the propagation of the

electron can be described as a classical trajectory [20]. As the name suggests the strong-field photoemission process can be divided into three sections.

1. Tunneling of the electron through the potential barrier.

2. Acceleration of the electron. As the electron moves in an oscillatory field also the electron motion will be of oscillatory nature and the electron will return to the parent ion.

3. Interaction of the electron and the parent ion.

These three steps are schematically shown in Fig. 2.5. The interaction of the electron with its parent ion in the last step can take different forms. Firstly, the electron can get elastically scattered from the parent ion. It then propagates away from the ion as a photoelectron in the opposite direction. There are also electrons emitted before the peak of the electric field whose trajectories do not cross the path of the parent ion again. These electrons that leave the atom without another interaction are called direct electrons. Secondly, the electron can recombine with the parent ion leading to the emission of a highly energetic photon whose energy is equal to the sum of the ionization potential and the kinetic energy of the recolliding electron. This process is the foundation of high harmonic generation (HHG).
The ionization process lifts an electron from a bound core state into the continuum where it has no initial velocity. To describe the propagation the strong-field approximation (SFA) is used. In the SFA, the Coulomb field of the ion is neglected and only the electric field of the laser is used to describe the motion. The equation of motion for the classical electron is

$$\frac{\mathrm{d}\vec{v}}{\mathrm{d}t} = -\frac{e}{m}\vec{E}\left(\vec{r},t\right). \tag{2.38}$$

For a homogeneous field $\vec{E}\left(\vec{r},t\right) = \vec{E}\left(t\right)$ is only dependent on time and the equation of motion can be solved straight-forwardly. The velocity for an electron emitted at t_0 is given as

$$\vec{v}\left(t,t_0\right) = \frac{e}{m}\left(\vec{A}(t) - \vec{A}(t_0)\right) + \vec{v}(t_0), \tag{2.39}$$

with the vector potential $\vec{A}(t) = -\int\limits_{-\infty}^{t} \mathrm{d}t'\vec{E}(t')$ and the initial velocity $\vec{v}(t_0)$ which is set to zero as the electron is emitted at rest. The electron position can be calculated by integrating the velocity over time and it is given by

$$\vec{r}\left(t,t_0\right) = \frac{e}{m}\left(\vec{B}(t) - \vec{B}(t_0) - \vec{A}(t_0)\left(t-t_0\right)\right), \tag{2.40}$$

with $\vec{B}(t) = \int\limits_{-\infty}^{t} \mathrm{d}t'\vec{A}(t')$. The recollision occurs at the condition $\vec{r}(t_r,t_0) = \mathbf{0}$ with a rescattering time $t_r > t_0$. For a linearly polarized pulse this equation can be reduced to one dimension and solved numerically.

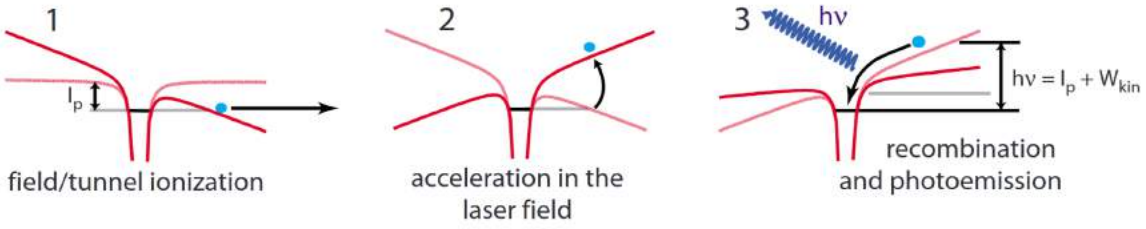

Figure 2.5: Schematic representation of the three-step model. In the first step the tunnel barrier is suppressed due to the electric field of the laser that heavily influences the atomic potential. The electron can therefore tunnel through the barrier and is accelerated away from the parent ion by the potential of the laser field. Due to the sinusoidal nature of the incoming laser field the potential changes the direction. The electron then gets accelerated into the opposite direction towards the parent ion. The third step is the recollision of the parent ion with the electron leading to the recombination and the following emission of the photon or a scattering event of the electron. Reprinted figure with permission from [22] ©2008 by the American Physical Society.

The different trajectories of the emitted electrons are shown in Fig. 2.6 where the green trajectories are from direct electrons not returning to the parent ion because the emission process takes place before the peak of the electric field. The other electrons return after approximately 3/4 of an optical cycle close to the zero-crossing of the field. The dashed line shows the most energetic trajectory that occurs shortly after the peak of the electric field and leads to reflected electrons with an energy of $E_{\mathrm{max}} \approx 10U_{\mathrm{p}}$ [21]. In general the elastically rescattered electrons can reach higher kinetic energies than the direct electrons because they get accelerated in the electric field again after elastic rescattering while starting at the velocity they already gained in the motion away from the parent ion and back.

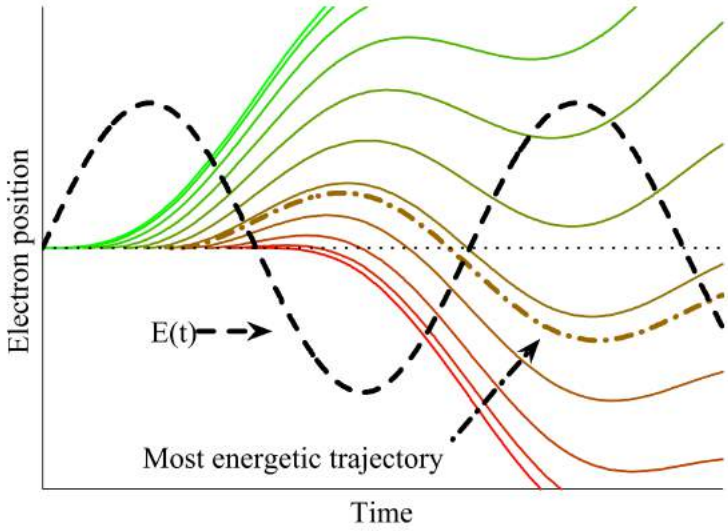

Figure 2.6: Trajectories for electrons ejected at different points in time of the cycle of the electric field. The green trajectories are formed by electrons emitted before the peak of the electric field. These are the so called direct electrons that do not return to the parent ion. Electrons created at the peak or afterwards can recollide with the parent ion and scatter or emit a photon. Illustration adapted from [23].

Chapter 3

Experimental Methods and Setup

This chapter describes the experimental setup and methods used to conduct the experiments in this thesis. Firstly, the laser system and the beamline located at the Max Planck Institute of Quantum Optics in Garching are discussed. A major part of this thesis consisted in the build-up of the experimental chamber. Secondly, the hollow core fiber used to generate the ultrabroadband pulses is described. Finally, the experimental methods for the measurement of the electric field oscillations used in this thesis, tunneling ionization with a perturbation for the time-domain observation of an electric field (TIPTOE) and nonlinear photoconductive sampling (NPS), are introduced in this chapter.

3.1 Experimental Setup

3.1.1 Lasersystem

The generation of the ultrashort pulses can be divided into three steps. Firstly pulses are generated in a Ti:Sapphire oscillator. These pulses are then amplified in a chirped-pulse amplifier (CPA) and spectrally broadened and further compressed in a hollow core fiber system. The different parts of the system are described in more detail in the following based on the explanations in [24] and [25]. A schematic representation is shown in Fig. 3.1.

Oscillator

The ultrashort pulses are generated in the Kerr-lens passively mode-locked Ti:Sapphire (Ti:Sapph) oscillator. The oscillator is pumped by a continuous wave (CW) frequency-doubled neodymium yttrium vanadate (Nd:YVO_4) laser emitting at a central wavelength of $\lambda = 532$ nm (Coherent, Verdi V6). Pumping the Ti:Sapphire crystal and mode-locking the laser leads to the generation of a pulsed laser emission at a repetition rate of $f_{\mathrm{rep}} = 78$ MHz with an average power of $P = 160$mW. The full width half maximum duration of the pulses is $\tau_{\mathrm{FWHM}} = 7$ fs with a pulse energy of $E_{\mathrm{pulse}} = 2.5$ nJ. The spectrum stretches

from $700 - 1000$ nm. The output pulses are focused into a periodically-poled lithium-niobate crystal (PPLN) for difference-frequency generation (DFG) between the high and the low end of the spectrum. The overlap of the spectrum of the fundamental pulse and the spectrum of the DFG signal leads to a CEP-dependent f-to-0 interference beat signal in the infrared (IR) that is monitored with a photodiode and a spectrum analyzer. The beat signal is used in the fast-feedback CEP stabilization loop controlling the acusto-optical modulator (AOM) that allows the fast modulation of the output power of the pump laser.

Chirped-pulse amplifier (CPA)

For the field sampling methods used in this thesis the generation of charge carriers, i.e. via tunneling ionization, is necessary. This requires a strong electric field and therefore the pulses generated from the oscillator have to be amplified. The prominent technique used for the amplification is chirped pulse amplification (CPA) and was introduced in the mid-1980s by Donna Strickland and Gérard Mourou [26], who received the Nobel prize in Physics in 2018 for this work. In this scheme, before the amplification process the pulses are chirped and stretched in the time domain which reduces the peak power of the pulses. The pulses are then amplified in a multi-pass cell. Due to the reduced peak power even the amplified pulses do not reach intensities that could lead to damage in the gain medium. After the amplification stage the pulses are compressed by correcting for the previously introduced chirp.
In our laser system, a block of fused silica (SF57) of the length $l = 13.5$ cm is used to introduce a positive chirp to the pulses of the collimated beam and stretch their duration to $\tau_{\mathrm{FWHM}} = 17$ picoseconds (ps, 1 ps $= 10^{-12}$ s). The stretched pulse is then amplified in a multi-pass amplifier based on a Ti:Sapphire crystal that is placed inside an evaporation cooled vacuum chamber at $T_{\mathrm{K}} = 177$ K. The pump laser in this system is a frequency-doubled neodymium-doped ytterbium lithium fluoride (Nd:YLF) laser (Photonics Industries, DM 30) that emits at a wavelength of $\lambda = 527$ nm with a power of $P = 30$ W and a repetition rate of $f_{\mathrm{rep}} = 4$ kHz. The duration of these pulses is in the nanosecond range.
The windows of the vacuum chamber are at Brewster angle to minimize the losses from reflection. After 4 passes through the crystal at the repetition rate given from the oscillator the pulse train is sent to a Pockel's cell that reduces the repetition rate to $f_{\mathrm{rep}} = 4$ kHz by picking out single pulses from the pulse train. The Pockel's cell makes use of the electro-optical effect that modifies or produces birefringence in a crystal by applying an electric field. Furthermore, the pulses are sent through a dazzler (Fastlite) that corrects for higher order phase distortions and pre-compensates gain-narrowing and therefore optimizes the amplification by introducing shorter and cleaner pulses. The pulse train at the new repetition rate passes the crystal 5 more times which results in a total of 9 passes.
After the amplification process the pulses have a pulse energy of $E_{\mathrm{Pulse}} = 1$ mJ which results in an average power of $P = 4$ W. The beam is collimated afterwards, stabilized and sent to a transmission grating compressor that introduces a negative dispersion to compensate for the positive dispersion introduced before the amplification process. The pulse is re-compressed to a duration of $\tau_{\mathrm{FWHM}} = 20$ fs close to the Fourier limit possible with

this spectral width. The shortest possible duration of the pulse is now long in comparison to the 7 fs pulses generated in the oscillator. This is a result of the fact that the amplification medium has a limited gain bandwidth and therefore the central spectral region of the pulse experiences a higher gain than the spectral wings. This leads to a decrease in the spectral bandwidth and therefore the Fourier-limit for the duration of the pulse increases. Furthermore, the pulse is no longer a few-cycle pulse at this point due to its time span.

Hollow-core fiber (HCF)

To shorten the pulses it is necessary to broaden the spectrum as is evident from the time-bandwidth product (Eq. (2.10)). This is achieved in a hollow core fiber (HCF) system. The beam is focused into the entrance of the HCF with a lens and its position is stabilized to avoid damage of the entrance. The fused silica fiber is 1.5 m long and has a core diameter of 250 μm. It resides inside a tube system that can be evacuated and is filled with neon at a pressure of $p = 1.6$ bar. The windows of the tube are at Brewster angle to minimize the losses from the reflection. The nonlinear interaction of the pulses with the noble gas lead to SPM and therefore the spectrum is broadened and a positive chirp is introduced. The output spectrum of the HCF ranges from the visible (VIS) to the near infrared (NIR) ($450 - 1050$ nm) with a central wavelength of $\lambda = 780$ nm. After the fiber the pulse is compressed again by 8 negatively chirped mirrors compensating for the dispersion in the HCF and precompensating for the following vacuum entrance window. The interaction in the HCF reduces the pulse energy by approximately half so the power after the fiber is $P_{\mathrm{HCF}} = 1.8$ W. The spectrum created in the HCF is shown in Fig. 3.2. The chirped mirrors futhermore change the spectrum used for the experiments as they cut off all wavelengths below 450 nm.
In front of the chirped mirrors there is a pair of wedges to control the amount of glass and therefore positive dispersion in the beam path.
The first reflection from the glass is used to generate the second harmonic of the spectrum after the fiber in a beta-barium borate (BBO) crystal. The blue part of the fundamental spectrum interferes with the second harmonic of the red part from the fundamental spectrum and the interference fringes are recorded with a spectrometer. This so-called f-to-2f-interferometer is used as an input signal in the slow feedback loop to detect slow drifts in the CEP and correct for them by controlling glass wedges inside the stretcher in front of the CPA.

3.1.2 AS4-Beamline

A schematic representation of the AS4-beamline is shown in Fig. 3.6. The setup was built and automatized mainly in the course of this thesis by the author. The whole setup resides in vacuum as the UV-pulses would get easily absorbed in air. For the electric field sampling an interferometer with two separate paths is used. Therefore, after a telescope narrows the beam, the beam is split by a perforated mirror (PFM). The inner part, going through the perforated mirror, is focused by a parabolic mirror into a target that can either be a

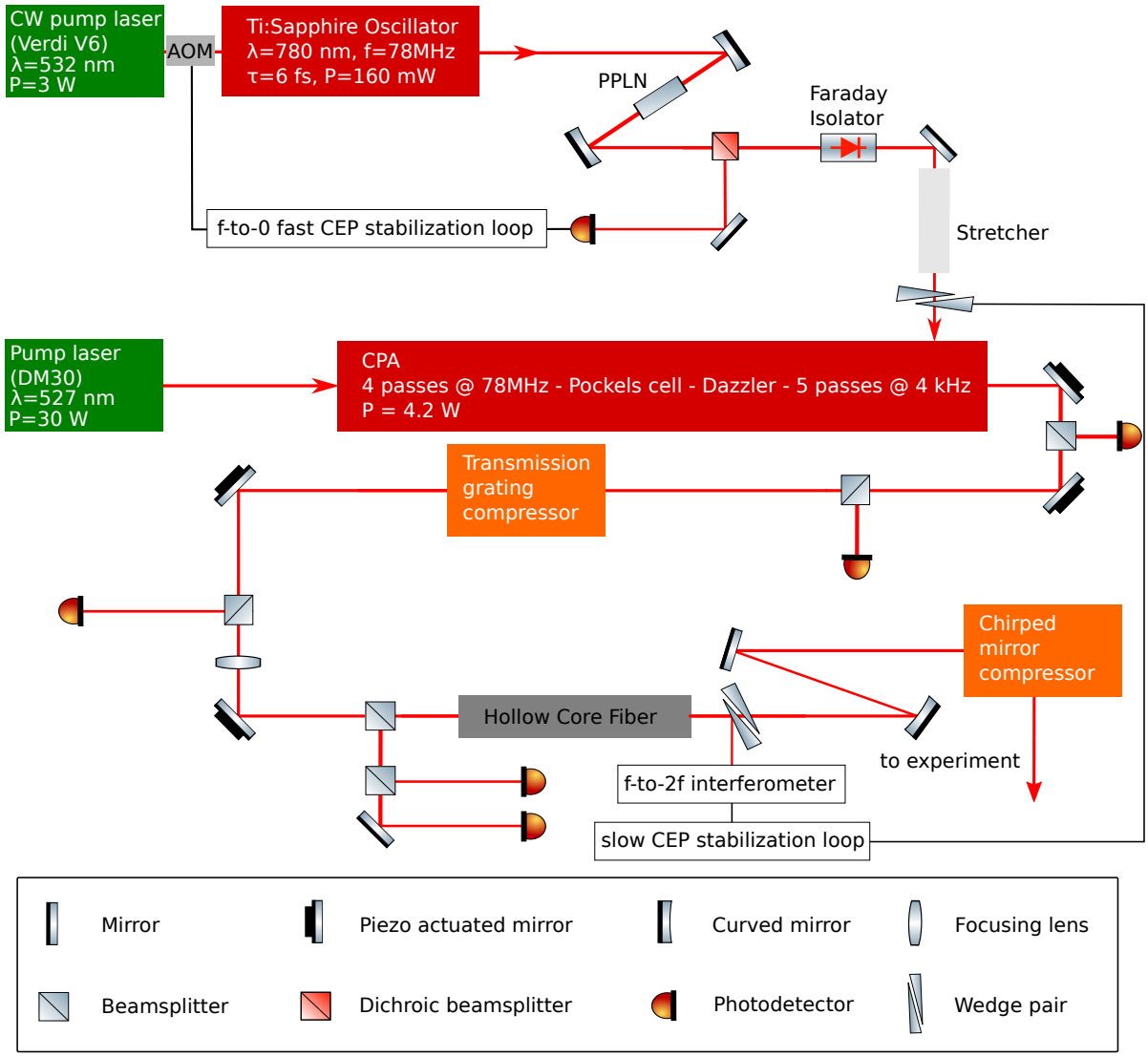

Figure 3.1: Schematic representation of the laser system. The Ti:Sapphire oscillator is pumped by a cw frequency-doubled Nd:YVO_4 laser whose output power is controlled by an acusto-optic modulator controlled by the f-to-0 fast CEP stabilization loop. The ultrashort pulses are focused into the PPLN, where a DFG signal is generated whose interference with the fundamental spectrum is the input of the fast loop. The beam is then sent through a Faraday isolator and passes the glass block that acts as the stretcher for the CPA twice before entering the CPA. The CPA reduces the repetition rate of the pulse train and amplifies the power of the pulses. The pulses are compressed again in a transmission grating compressor. The pulse is then focused into the HCF and afterwards compressed by a set of eight chirped mirrors before being sent to the experiment. The graphic representation is adapted from [24]

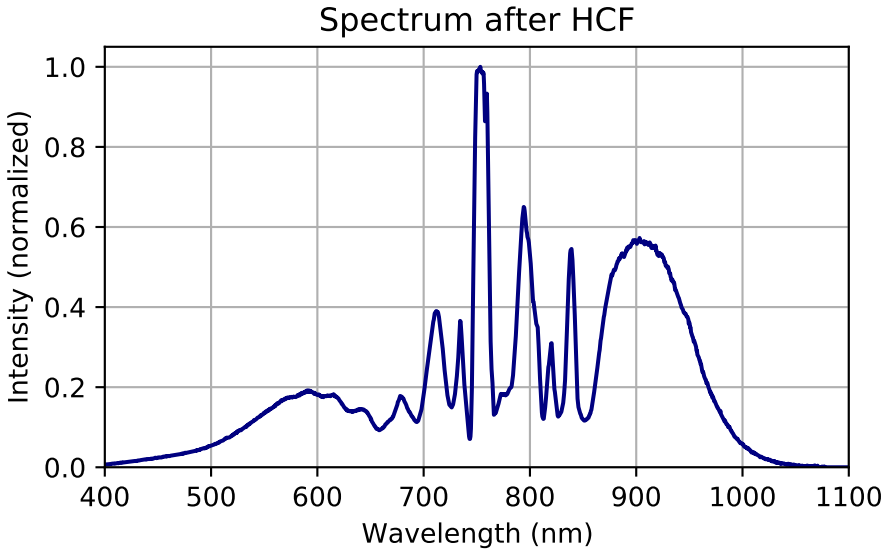

Figure 3.2: Spectrum after the hollow core fiber. The chirped mirrors after the HCF influence the spectrum as they cut off all wavelengths below 450 nm. This modulated spectrum is used for the experiments conducted in the AS4-beamline. Furthermore it is used as the input spectrum in the simulations.

hollow core fiber that can be filled with gas, a gas target or a fused silica plate.
The HCF is used to generate the deep UV pulses by the mechanisms of SPM and self-steepening. This is explained further in the next section. The beam is then re-collimated. A mirror can be inserted into the beam to lead it outside the vacuum chamber through a window. The beam is then focused into a UV-sensitive spectrometer (Ocean Insight Maya2000 Pro) that detects in the wavelength range $\lambda = 155 - 305$ nm.
When the mirror is removed, depending on which measurement technique for the field-resolved measurements is used, there is a chopper in the beam path that blocks every second pulse. Furthermore, a periscope (periscope 2) changes the height of the beam. The periscope consists of two mirrors where each mirror can be a coated mirror or a silicon wafer reflecting at Brewster angle to absorb the infrared part of the spectrum. Furthermore, there is also a thin plate of fused silica that can be inserted into the beam to change the spectral phase of the pulses.
The delay between the different beam paths is controlled with a piezo stage (PI N-565) in the path of the outer part that is reflected off from the perforated mirror. Furthermore the polarization of the beam can be controlled with the periscope. For the two sampling methods different polarizations with respect to the other beam are used. In the case of NPS the polarization is rotated about 90° to be perpendicular to the polarization of the other beam. TIPTOE measurements on the other hand are conducted with the same polarization in both beams. The two beams are recombined at another perforated mirror and get focused by a spherical mirror.

A glass wedge can be inserted into the beam path to reflect the beam into a UV-sensitive spectrometer (Resonance Ltd. VS7550 VUV Mini Spectrometer). The spectrometer is attached directly to the vacuum chamber to ensure that the beam does not propagate through a medium and therefore the UV does not get extinguished.
Furthermore, the electric field of the pulses is determined in the experiments in this thesis. The glass wedge is removed in this case and the beams are focused onto a spot between two electrodes. For the electrodes to measure a current, charge carriers must be generated through the ionization of a medium. In the experiments conducted in this thesis different media for the electrodes and the ionizing medium are used. One sample is copper-electrodes surrounded by air that is distributed by a gas nozzle close to the electrodes. The other sample is a pair of gold electrodes on a plate of fused silica. A typical sample used in the experiments is shown in Fig. 3.3.
The small current signal at the electrodes is converted into a voltage signal by a transimpedance amplifier and read out by a lock-in amplifier [27]. A lock-in amplifier can filter out a signal from a noisy background by using the knowledge about the signal's time dependence. The modulation of the input signal at a frequency f_{ref} is caused by changing the CEP or by an optical chopper. The signal $V_{\mathrm{s}}(t)$ is then split up in the lock-in amplifier and once multiplied with the sinusoidal reference signal and once with a 90° shifted copy of the reference signal.
After passing the electrodes the overlapping beams are sent out of the vacuum chamber through a glass window and can be sent to a camera or a spectrometer. The camera is used to find the spatial overlap of the two beams. The beamprofiles of the two beams that can be seen on the camera are shown in Fig. 3.4. It can be seen that the focus of the beam passing the fiber (right) is larger as the collimated beam is smaller than the other beam due to the passage through the center of the perforated mirror. The other collimated beam (left) is reflected from the perforated mirror and therefore is larger in size which leads to a smaller focus size.
The spectrometer can be used to check the temporal overlap of the pulses that is adjusted via the length of the arm that does not include the fiber via the delay stage. The resulting output of the spectrometer is displayed in Fig. 3.5. Close to the point of the temporal overlap the interference of the two spectra can be seen as fringes. If the length of the paths is adjusted more closely to the length of the temporal overlap, the wavelength of the interference fringes increases and decreases again when passing the length of temporal overlap. This point is used as the center of the for the sweep over the difference in length between the two interferometer arms that is performed in the methods for the field-resolved measurements.

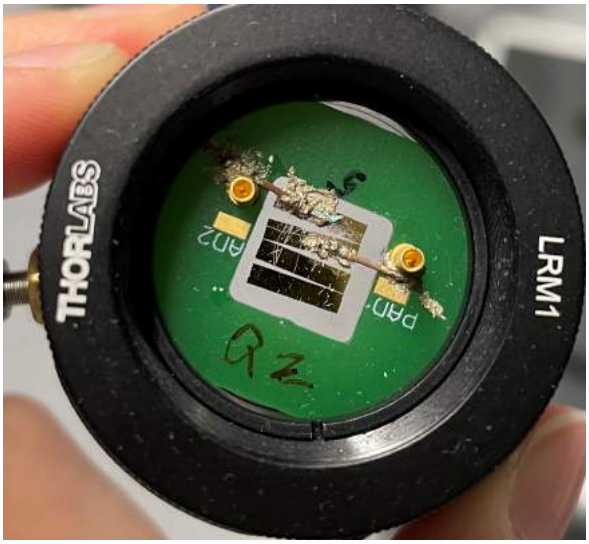

Figure 3.3: Image of the fused silica sample to conduct NPS and TIPTOE measurements. The electrodes of this sample consist of gold and the medium that gets ionized is fused silica. This sample allows for the variation of the distance between the electrodes.

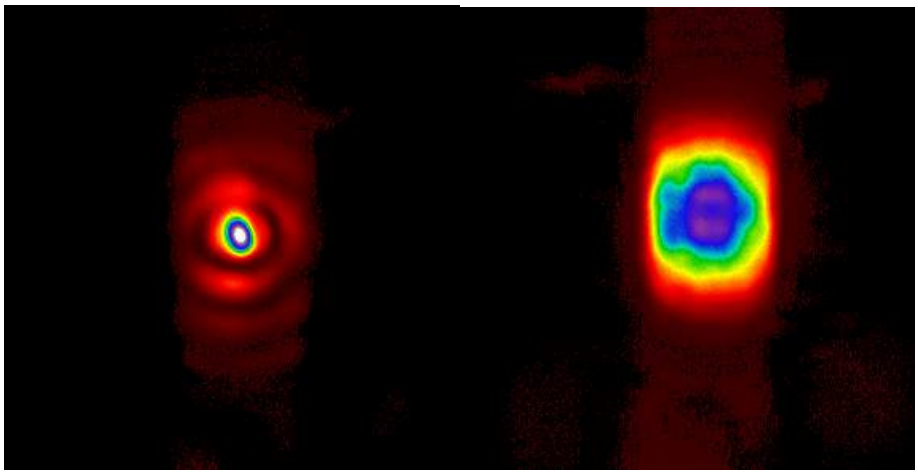

Figure 3.4: Beamprofile images of the beam that passes the fiber (right) and the other interferometer arm (left). The beams are centered between the two electrodes that can be seen as the black areas on the left and the right side of the images. The focus size of the two beams varies due to the different sizes of the collimated beams depending on whether they pass through the center (beam that passes through the fiber) or are reflected from the perforated mirror.

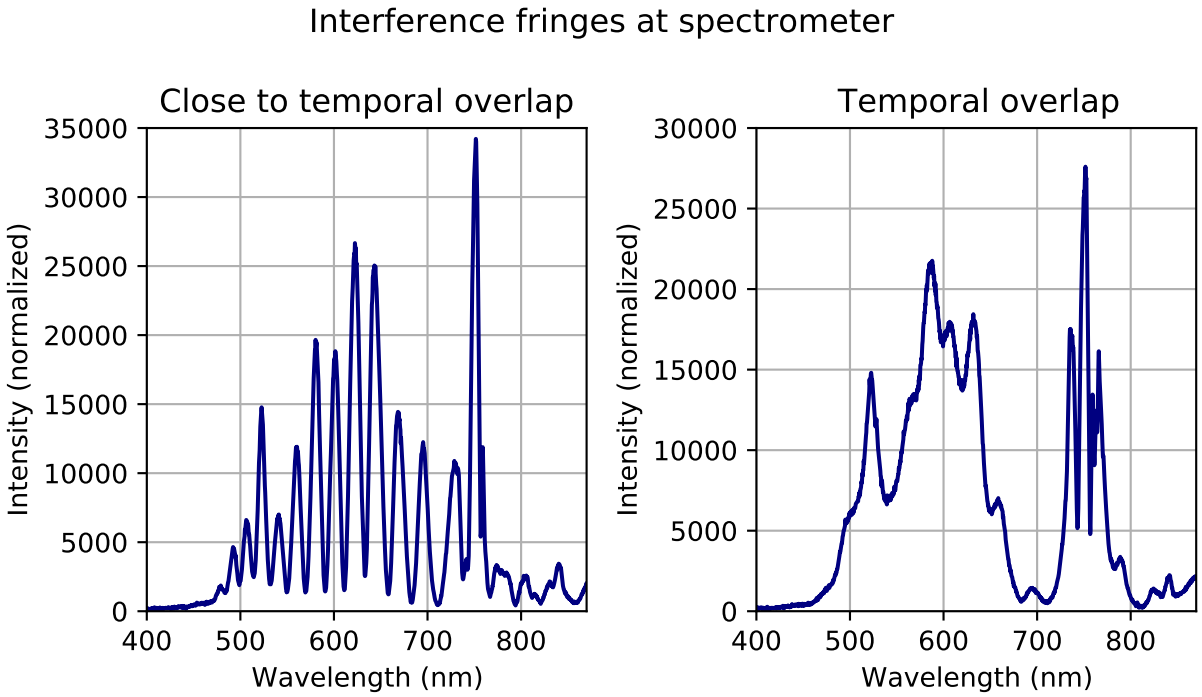

Figure 3.5: Spectral interference of the two interferometer arms. Close to the point of the temporal overlap the interference of the two spectra can be seen as fringes. If the length of the paths is adjusted more closely to the length of the temporal overlap, the wavelength of the interference fringes increases, as can be seen on the image on the right side.

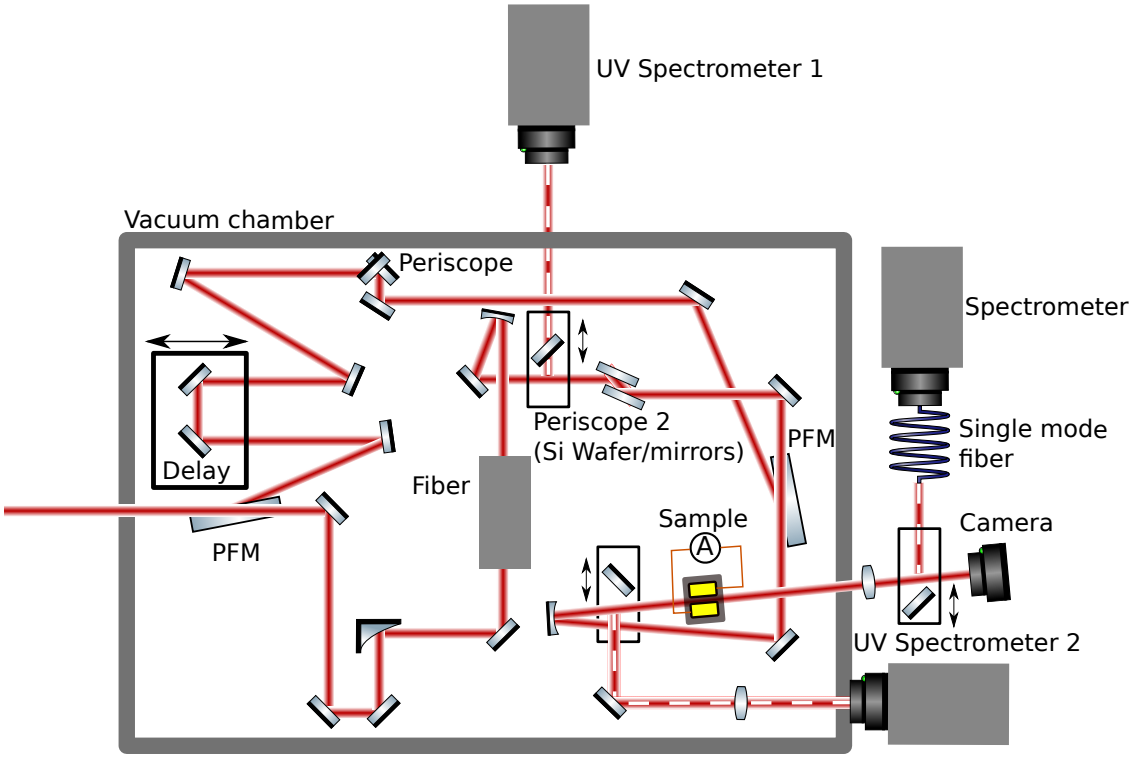

Figure 3.6: Schematic representation of the AS4-beamline. The beam is split at the first perforated mirror. The inner part of the beam is focused into a hollow core fiber, collimated afterwards and the intensity is lowered due to the Silicon wafers. The path length of the outer part of the beam can be adjusted with the delay stage. Furthermore the polarization of the beam can be changed with the periscope construction. The beams are overlapped at the second perforated mirror and are then focused onto a sample where currents can be measured for the NPS or the TIPTOE method. The focus is imaged onto a camera or into a single mode fiber that is connected to a spectrometer. There are two UV-sensitive spectrometers. The beam passing the fiber can be redirected out of the vacuum chamber to reach the UV spectrometer 1. Furthermore, one or both beams can be focused into the UV spectrometer 2 that is connected directly to the vacuum chamber. The image is adapted from [28].

3.2 Hollow Core Fiber (HCF)

The aim of this thesis is to generate ultrabroadband continuum radiation covering the deep ultraviolet (DUV) ($\lambda = 200 - 300$ nm) and reaching down into the vacuum ultraviolet (VUV) ($\lambda = 100 - 200$ nm) to $\lambda \approx 160$ nm. This is achieved in a fused silica hollow core fiber (HCF) in the AS4-beamline using the output from the FP3 laser system. The length of the fiber can be chosen between 2.5 cm and 5.5 cm with a core diameter of $2a = 100$ μm at both lengths. The HCF is filled with argon at variable pressure that is inserted by two tiny holes in the cladding. The fiber is fixed in a construction that allows the gas to enter through the holes and exit through the core endings. The holes are located at the end of the fiber so the pressure in the center can be assumed to be constant. The design of the fiber holder is shown in Fig. 3.7. The spectrum of the pulses is broadened via self-phase modulation (see section 2.2.2 Self-phase modulation (SPM)) and is recorded with a UV-spectrometer. Furthermore the electric field is recorded with NPS or TIPTOE. The spectrum can be calculated from the electric field trace with the Fourier transformation. The field sampling techniques are explained in more detail below.

3.2.1 Simulation

The nonlinear interaction of the pulses with the gas in the fiber can additionally be simulated. In this thesis the python package pyNLO [29] is the program used for the simulation. The program calculates the propagation of a laser pulses by computing the time and frequency representation at small distances in the fiber. Therefore the generalized nonlinear Schrödinger equation (GNLSE) that takes the following form when neglecting contributions from the delayed Raman response [30]

$$\frac{\partial A}{\partial z} = -\frac{\alpha}{2}A - \left(\sum_{n=2}^{\infty} \beta_n \frac{i^{n-1}}{n!}\frac{\partial^n}{\partial T^n}\right) A + i\gamma\left(1 + \frac{1}{\omega_0}\frac{\partial}{\partial T}\right) A|A|^2, \tag{3.1}$$

where α is the attenuation coefficient, β_n are the higher order dispersion coefficients introduced in section 2.1.2 Dispersion and γ is the nonlinear parameter. The first two terms on the right-hand side describe the fiber loss and the dispersion, respectively. The last term is responsible for the nonlinear optical phenomena.
For the propagation in a gas filled hollow core fiber the attenuation coefficient takes the form [31]

$$\alpha = 2\left(\frac{u_{nm}}{2\pi}\right)^2 \frac{\lambda_0^2}{2a^3}\frac{\nu^2+1}{\sqrt{\nu^2-1}}, \tag{3.2}$$

with u_{nm} the m^{th} root of the Bessel function J_{n-1} and λ_0 the central wavelength of the laser pulse. Furthermore, a is the core radius of the fiber and $\nu = \frac{n_{fiber}}{n_{gas}}$ is the ratio of the refractive indices of the external (fused silica) and internal (gas) media, respectively. The nonlinear parameter is defined as

$$\gamma = \frac{n_2\omega_0}{cA_{eff}} \tag{3.3}$$

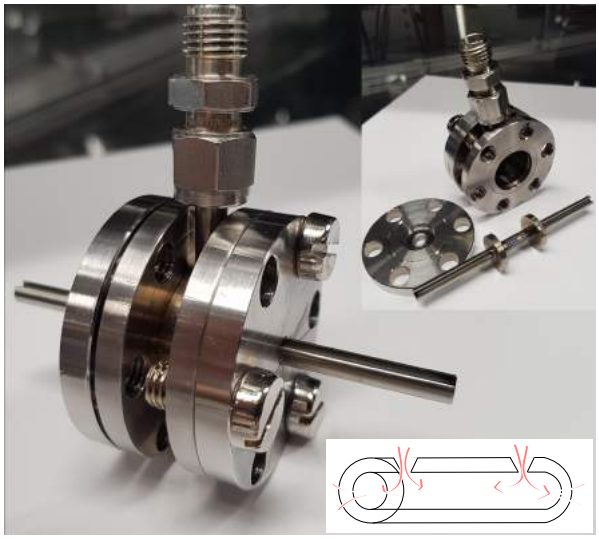

Figure 3.7: Image of the fiber holder. The fused silica fiber is glued into a metallic holder. The gas enters through the two holes in the fiber and exits at the core endings as seen in the schematic sketch.

with the nonlinear refractive index n_2 (see section 2.2.1 Kerr effect), the central pulse frequency ω_0, the speed of light c and the effective mode area $A_{eff} \approx 0.48\pi a^2$.
The refractive index depends on the pressure and the temperature of the gas as follows [32]

$$n_2 = n_2^0 \frac{p}{p_0} \frac{T_0}{T} \tag{3.4}$$

with $p_0 = 1$ bar and $T_0 = 273$ K. Furthermore, the refractive index is frequency depended and can be calculated as [33]

$$n_2^0(\omega) = \frac{\nu'\omega' - \omega_p}{\nu'\omega - \omega_p} n_2^0(\omega'), \tag{3.5}$$

where $\nu' = \frac{3}{2}$, and the angular frequency connected to the ionization potential ω_p and the reference refractive index at $\lambda = 800$ nm is given in [33].
The dispersion is given as [32]

$$\beta(\omega) = \frac{\omega}{c} \sqrt{n_{gas}^2 - \frac{u_{nm}^2 c^2}{a^2 \omega^2}} \tag{3.6}$$

with the nonlinear index of the gas calculated via the Sellmeier equation, where the gas dependent parameters B_i and C_i are given in [34]

$$n_{gas}^2 - 1 = \frac{p}{p_0} \frac{T_0}{T} \left[\frac{B_1 \lambda^2}{\lambda^2 - C_1} + \frac{B_2 \lambda^2}{\lambda^2 - C_2} \right]. \tag{3.7}$$

To solve the GNLSE for every step, a fourth-order Runge-Kutta algorithm in the interaction picture is applied [30]. The pyNLO package used in this thesis is a version modified

by Michael Heynck [35]. To calculate the coefficients α and γ Eq. (3.2) and Eq. (3.3) are used. These parameters are wavelength dependent but in the simulation they are treated as constants and calculated only for the central wavelength of the pulse. Furthermore, the program was modified to use Eq. (3.6) instead of calculating the β-coefficients independently. The parameters used in the experiment can be recreated in the simulation. The spectrum measured after the chirped mirrors is used as the input spectrum in the simulation.

3.3 Field Sampling

Knowledge of the electric field trace of an ultrashort pulse enables the investigation of events on the time scale of an electric field oscillation. In this thesis tunneling ionization with a perturbation for the time-domain observation of an electric field (TIPTOE) and nonlinear photoconductive sampling (NPS) are used to measure the electric field of electro-magnetic pulses. Both field sampling techniques measure a current at two electrodes induced from free charge carriers created from the ionization of a gas or solid state material. The two techniques are described further in the following. The explanation closely follows [16].

3.3.1 Tunneling ionization with a perturbation for the time-domain observation of an electric field (TIPTOE)

Tunneling ionization with a perturbation for the time-domain observation of an electric field (TIPTOE) was introduced by Park et al. in 2018 [1]. The strong field of the pump pulse $E_{\mathrm{F}}(t)$ induces tunneling emission constituting a sub-cycle temporal gate at around $t_0 = 0$. The pulse to be measured is the weak time-delayed perturbing signal field $E_{\mathrm{s}}(t)$ with the same polarization as the pump pulse. The chopper is used in this setup to reduce the frequency of the signal pulses by half so the signal field is only present in every other pulse and the difference between only the pump pulse and the pump pulse plus the signal pulse is measured by the lock-in amplifier. The tunneling emission rate is modified by the signal pulse and depending on whether the electric field of the signal pulse points in the same or the opposite direction as the electric field of the pump pulse the emission rate is increased or decreased, respectively.
The tunneling emission rate of the combined signal can be approximated with a Taylor approximation up to the first order where the signal electric field is treated as a small perturbation to the pump field E_{F}

$$w(E_{\mathrm{F}}(t-\tau)+E_{\mathrm{s}}(t)) = w(E_{\mathrm{F}}(t-\tau)) + \frac{\mathrm{d}w(E)}{\mathrm{d}E}|_{E_{\mathrm{F}}(t-\tau)} E_{\mathrm{s}}(t). \tag{3.8}$$

τ is the time delay of the signal pulse compared to the pump pulse. The first part on the right handside of this equation is the emission rate without the perturbation of the signal field and the second part is interpreted as the cross-correlation of the gating function with the gating field [36]. The emitted charge can be calculated as the integral of the emission

rate over the pulse duration. Furthermore the gating function for the tunneling emission burst at a time t_0 can be approximately described as a delta-function $\delta(t-\tau-t_0)$. The change in the emitted charge ΔQ due to the presence of the signal field is then

$$\Delta Q(\tau) \propto \int \frac{\mathrm{d}w(E)}{\mathrm{d}E}|_{E_\mathrm{F}(t-\tau)} E_\mathrm{s}(t)\mathrm{d}t \propto \frac{\mathrm{d}w(E)}{\mathrm{d}E}|_{E_\mathrm{F}(t_0)} E_\mathrm{s}(t_0+\tau). \tag{3.9}$$

The change in charge emission is therefore approximately proportional to the strength of the signal electric field if there is only one emission burst. If there are several emission bursts, the gating function becomes the sum of delta-functions with their peaks at the times of their respective bursts. The occurrence of two dominating equal emissions can furthermore lead to a CEP-dependence of the spectral response function for few-cycle pulses as the emission modulation of the two bursts can counteract [36]. If the pump and signal pulse originate from the same laser source the TIPTOE measurement can be conducted without CEP-stabilization as the relative phase of the pulses does not change.
In the original work gas was used as the ionizing medium [1] and the technique was used for the characterization of an optical near-single-cycle pulse [37] and multi-cycle laser pulses from the IR to the UV [38]. In the experiments conducted in this thesis air and fused silica are used as the ionizing medium.

3.3.2 Nonlinear Photoconductive Sampling (NPS)

Optical fields inducing currents in dielectrics was demonstrated in 2013 by Schiffrin et al. [39] and has since influenced the advancement in attosecond science. Electrons are lifted from the valence to the conduction band in a nonlinear transition induced by a strong-field laser pulse which increases the conductivity. Additionally, a focused strong-field laser pulse leads to nonlinear ionization of a medium between two electrodes. If the pulses are polarized parallel to the electrodes, the charge carriers are driven towards the electrodes and a current is induced. CEP-dependent measurements can be conducted by flipping the CEP between consecutive pulses by $\Delta\phi_\mathrm{CEP} = \pi$.
Nonlinear photoconductive sampling in solids for the field-resolved measurement of UV to MIR pulses based on the same approach was introduced by Sederberg et al. in 2020 [2]. The configuration is changed such that there are two orthogonally polarized pulses as depicted in Fig. 3.9. The injection pulse is polarized perpendicular to the electrodes and is only used for the ionization that generates charge carriers. The driving pulse on the other hand is polarized parallel to the electrodes and induces a movement of the free carriers leading to a current that can be measured at the electrodes. The driving field $E_\mathrm{d}(t)$ is weak in comparison to the injection field and it is weak enough that the response is linear. In this case the measured signal can be calculated as the convolution [2]

$$S_\mathrm{d}(\tau) = -\int_{-\infty}^{\infty} A_\mathrm{d}(t)G(t-\tau)\mathrm{d}t \tag{3.10}$$

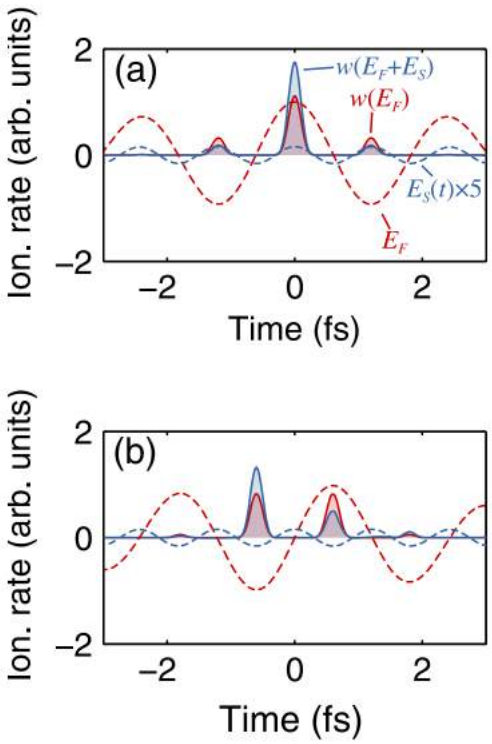

Figure 3.8: Calculated ionization rates (solid lines) of the fundamental field E_{F} (red) and the fundamental field including the signal field E_{s} (blue). The ionization rates are shown for a Gaussian cosine **(a)** and a Gaussian sine **(b)**. Reprinted with permission from [1] ©The Optical Society.

of the vector potential of the driving field $A_\mathrm{d}(t) = \int_t^\infty E_\mathrm{d}(t')\mathrm{d}t'$ with a gating function $G(t)$ that represents the excitation dynamics from the injection pulse and the physical processes for the formation and detection of the macroscopic dipole. Simulations show that the energy deposition in the material is approximately proportional to the eight power of the electric field for NIR-laser pulses and fused silica as the material, which is a highly nonlinear dependence. This indicates that carrier injection happens only in a small interval around the one or two highest extrema of the electric field of the injection pulse. The gating function can be approximated following the simulation results as

$$G(t) \propto E_\mathrm{i}^8(t - \tau_\mathrm{inj}), \tag{3.11}$$

describing its nearly instantaneous energy deposition and accounting for a small temporal displacement τ_inj.
In general the induced current is dependent on the time delay between the injection and the driving pulse. Variation of the time delay is used to reconstruct the driving pulse. In contrast to the TIPTOE technique no chopper is used and instead the CEP of the injection and the driving pulse is flipped by $\Delta\phi_\mathrm{CEP} = \pi$ between consecutive pulses. The NPS technique has been extended to media in the gas phase [40]. Solid materials used as ionizing medium in NPS are ionized close to the damage threshold. An advantage of using materials in the gas phase instead, is that no damage occurs. Furthermore the gas parameters, as for example the density, can be varied and their influence on the experiments can reveal further information about the mechanisms of the signal generation.

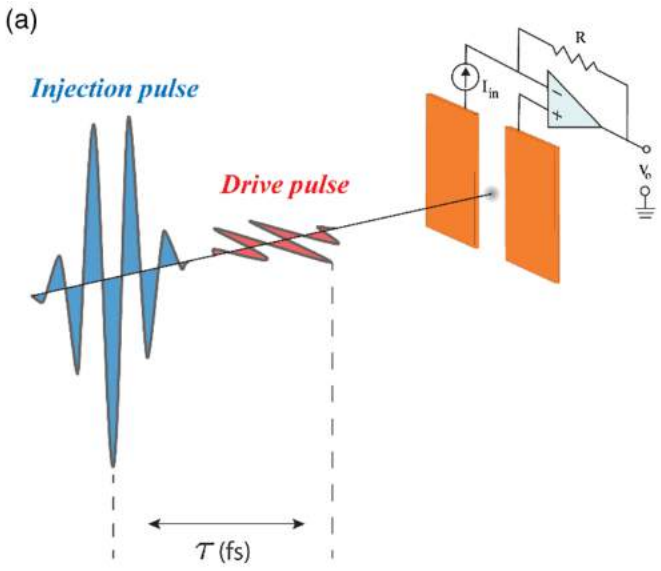

Figure 3.9: Schematic representation of the measurement setup for NPS. The strong injection pulse that ionizes the medium in between the electrodes and the weak driving pulse are polarized orthogonally. The signal from the electrodes is sent to a transimpedance amplifier that converts the current signal into a voltage signal that is read out by the lock-in amplifier. Reprinted with permission from [40] ©The Optical Society.

Chapter 4

Generation of an ultrabroadband spectrum

This chapter focuses on the generation of an ultrabroadband spectrum via self-phase-modulation in an argon-filled hollow core fiber. Firstly, the experimental measurement of the UV pulses is analyzed and the generation depending on the pressure of the gas in the fiber is evaluated. Secondly, the experimental results are compared to the simulation and the energy conversion efficiency of the generated pulses is investigated with the simulation. Finally, the experimental and simulated results are discussed collectively.

4.1 Ultrabroadband spectrum

One of the goals of this thesis is the generation of an ultrabroadband spectrum. The experimental setup is described in chapter 3. The laserpulses generated in the hollow core fiber in the FP3-setup which serve as the input pulses for our experiment reach from approximately 450 nm to 1050 nm (see Fig. 3.2). The goal of the thesis is to extend the spectrum further into the vacuum ultraviolet (VUV) down to approximately 160 nm covering the whole deep ultraviolet (DUV). These wavelengths are reached due the nonlinear optical processes, mostly self-phase-modulation (SPM), that take place when the strong electric field of the laser pulse interacts with the noble gas argon inside the hollow core fiber (HCF) located in the AS4-beamline (see section 2.2 Nonlinear optical phenomena).

4.2 Setup

There are two different setups and spectrometers that were used in this thesis to record the spectrum of the generated pulses. Firstly, a spectrometer not directly attached to the vacuum chamber (UV spectrometer 1 in Fig 3.6) is used. The disadvantage of this technique is that wavelengths below approximately 185 nm are absorbed very fast when passing through the air outside the vacuum chamber due to the absorption in oxygen. Secondly, the UV spectrometer 2 in Fig. 3.6 that is directly attached to the vacuum

chamber is used as a measurement device. In this case the spectrum is recorded loss-free as the pulses only propagate through vacuum and no dispersion- or absorption-effects take place.
The exact setup and the spectrometers are described in section 3.1.2 AS4-Beamline.

4.3 Experimental results

The first pressure dependence scan to check the generation of the ultrabroadband spectrum is conducted with the spectrometer outside of the vacuum chamber. The results are shown in Fig. 4.1. The pressure of the argon in the fiber is varied from 25 mbar (blue line) up to 1400 mbar (light blue line). The shorter fiber of 2.5 cm is used in this measurement. The power at the entrance of the fiber is measured to be approximately 200 mW which results together with a repetition rate of 4 kHz in a pulse energy of 50 μJ. The expansion of the spectrum of the pulses into the DUV is clearly measurable. Furthermore, the measurements show the predicted cutoff at $\lambda = 185$ nm independent of the pressure used in the fiber. This cutoff wavelength is determined by the absorption effects in oxygen. This is indicated by the discrete dips in the spectra between 185 nm and 195 nm that can be identified with the so-called Schumann-Runge absorption bands of diatomic oxygen [41].

To further investigate the spectra generated in the fiber, the second setup with a different UV-sensitive spectrometer that is directly attached to the vacuum chamber is used. As the vacuum chamber was constantly under construction, the parameters might slightly vary between this and the measurement above. The pulse energy of approximately 50 μJ is again measured via a power measurement. The results are shown in Fig. 4.2. As can be seen in the inset, the nonlinear interactions in the gas-filled fiber lead to the extension of the spectrum into the VUV down to $\lambda = 170$ nm. This is close to the wavelength region that was aimed to be generated. This goal can therefore be considered as having been achieved.
On a side note, the interference fringes between 400 nm and 450 nm can be understood as the result of the interference between the original spectrum and the spectrum generated from the nonlinear interaction in the fiber. The reason is that the chirped mirrors used to compress the input pulses, do not work below 450 nm and these spectral components are therefore delayed with respect to the pulse. The newly generated components in the second UV-broadening stage are, however, produced at the main peak. It is this temporal delay between the two spectral components that leads to interference fringes.

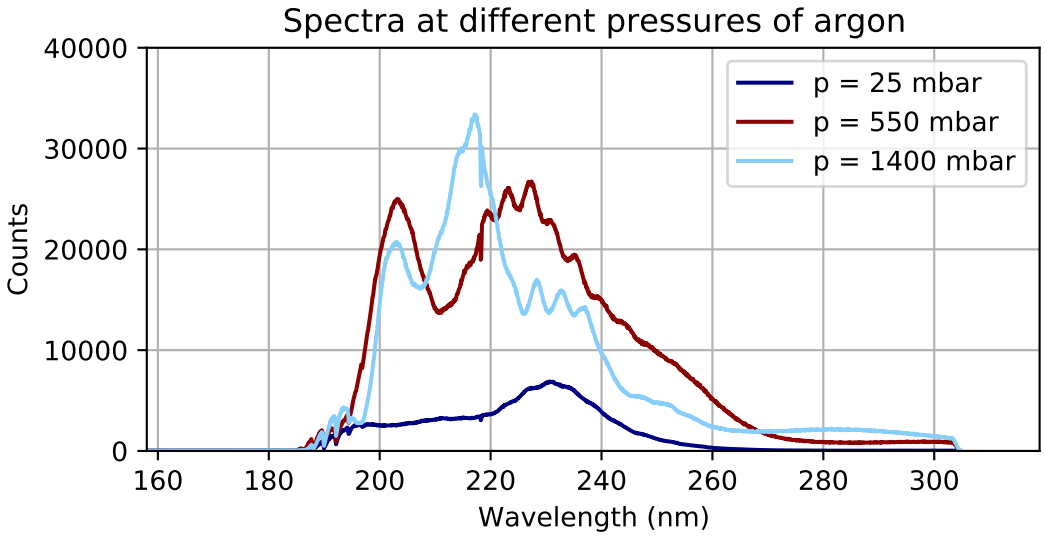

Figure 4.1: Pressure scan of the short fiber with the spectrometer outside of the vacuum chamber. The measured spectra for $p = 25$ mbar (blue line), $p = 550$ mbar (red line) and $p = 1400$ mbar (light blue line) with an integration time of $t_{\text{int}} = 25$ ms are shown. The wavelength limit of 185 nm due to the absorption of the VUV in oxygen is reached independent of the pressure. The discrete dips in the spectra between 185 nm and 195 nm can be identified with the so-called Runge-Schumann absorption bands of diatomic oxygen.

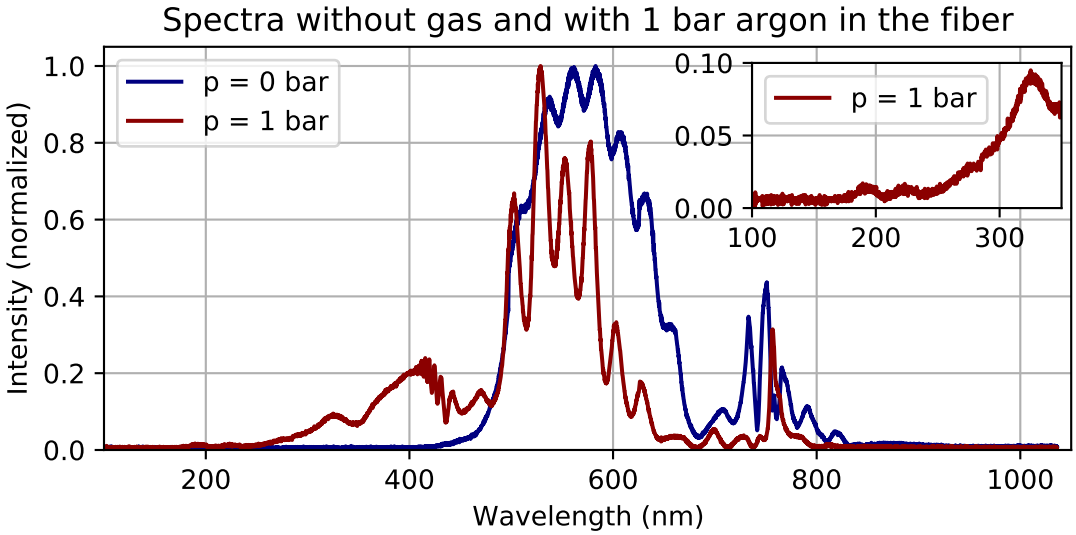

Figure 4.2: Measured spectrum with no gas in the fiber (blue line) and with argon at $p = 1$ bar (red line). With gas in the fiber the spectrum is extended into the VUV down to approximately 170 nm, as can be seen in the inset. Furthermore, interference fringes between 400 nm and 450 nm from the initial and the generated spectrum can be seen.

4.4 Simulation

The nonlinear interactions are also simulated with the program pyNLO that is described in section 3.2.1 Simulation. The propagation of an incident laser pulse that is defined via the input spectrum from the measurement shown in Fig. 3.2 through a fiber of variable length filled with argon at a variable pressure is simulated here. It is important to note that the data measured in the experimental setup is not exactly reproduced in the simulations done here. Nevertheless, simulations can help to better understand the experimental results and improve the VUV-generation process.
For a better comparison to the experimental data, Fig. 4.3 shows the simulated spectra for the same parameters that were used in the experiments shown above. Pulses of the energy 50 μJ (blue line) are propagated through the short 2.5 cm fiber at a pressure of 1 bar argon. To see the effect of a higher pulse energy, the same simulation is conducted with a pulse energy of 100 μJ (red line). It can be seen that the lower cutoff wavelength is shifted to smaller wavelengths for the use of higher pulse energies. Furthermore, the energy conversion efficiency can be calculated for both simulations. The conversion efficiency is calculated as the ratio of the energy contained in the UV spectral region $150 - 340$ nm and the energy contained in the whole spectrum. The conversion efficiencies are 14% and 28% for pulse energies of 50 μJ and 100 μJ, respectively. The conversion efficiency can therefore be increased with the use of a higher pulse energy.

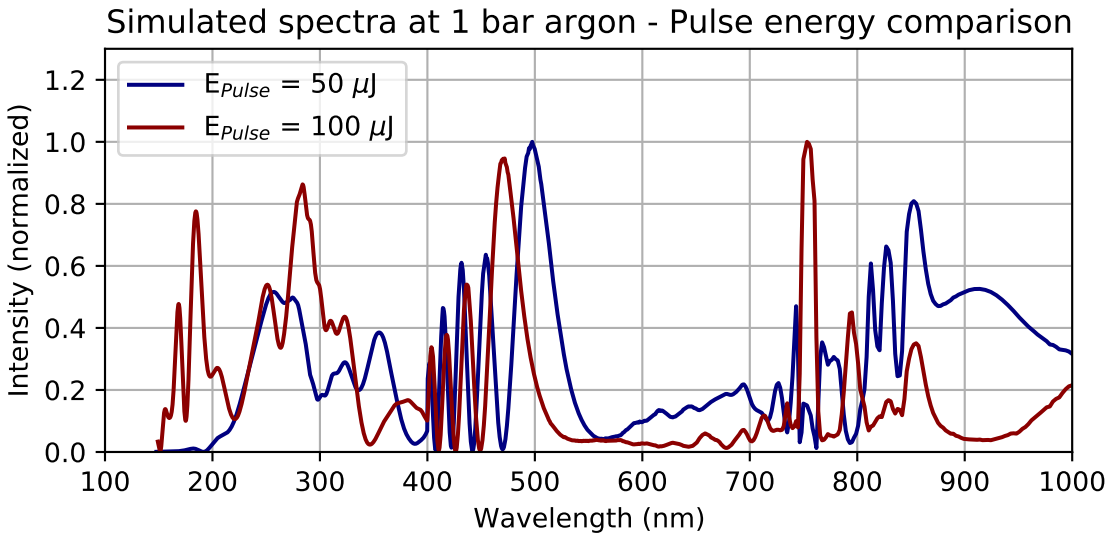

Figure 4.3: Spectral intensity acquired with pyNLO for the pulse passing the short fiber filled with argon at $p = 1$ bar. The simulation was done for the pulse energy $E_{\text{pulse}} = 50$ μJ (blue line) that was used in the experiments and the pulse energy $E_{\text{pulse}} = 100$ μJ (red line). The spectrum reaches further down the higher the pulse energy gets.

Furthermore, the pressure dependence of the generated spectrum was simulated. The results for a pulse with an energy of 50 μJ in the short 2.5 cm fiber filled with argon at pressures of 0.5 bar (blue line), 1 bar (red line) and 1.5 bar (light blue line) are shown in Fig. 4.4. Firstly, it can be seen that the wavelength cutoff in the UV is not affected by the pressure of the gas. Secondly, the energy conversion efficiency of the UV spectral region can be calculated with the results of the simulation as explained above. The conversion efficiency is increased if a higher pressure of argon is used in the fiber, namely the efficiencies are calculated to be 4%, 14% and 20% for the increasing pressure.
Fig. 4.5 shows the spectral intensity as a colorplot dependent on the propagation length through the fiber filled with $p = 1$ bar argon and a pulse energy of 50 μJ to look at the effect of longer fibers. The figure shows that the generation of spectral components in the region of 200 nm increases strongly at approximately 5 cm propagation length.

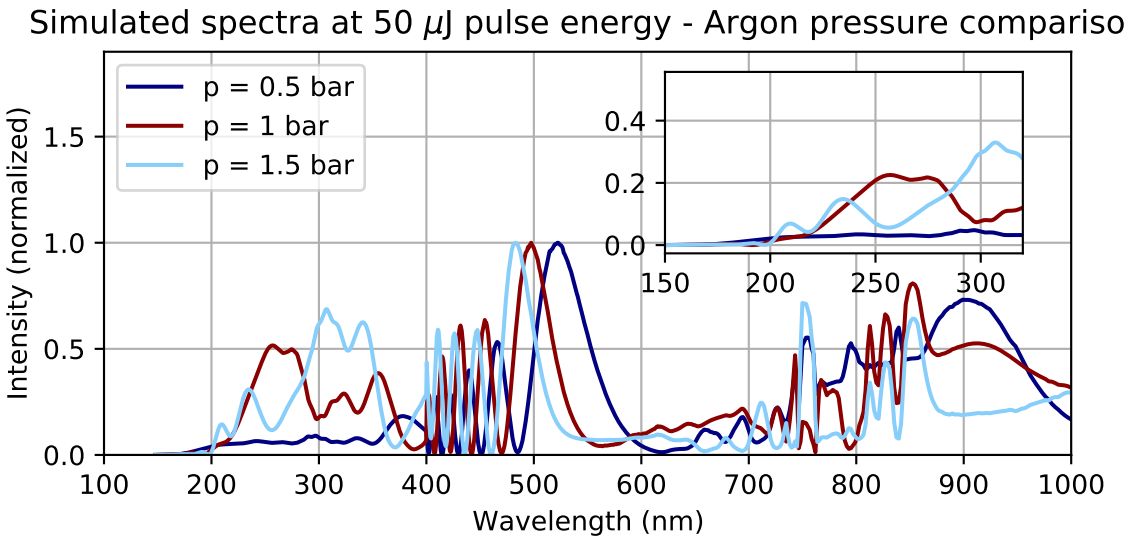

Figure 4.4: Spectral intensity acquired with pyNLO for a pulse energy of 50 μJ. The propagation is simulated through the short fiber of 2.5 cm filled with argon at 0.5 bar (blue line), 1 bar (red line) and 1.5 bar (light blue line). The cutoff wavelength is not influenced strongly by the variation of the pressure in the fiber. The energy conversion efficiency of the UV spectral region is increased with higher pressures of argon in the fiber.

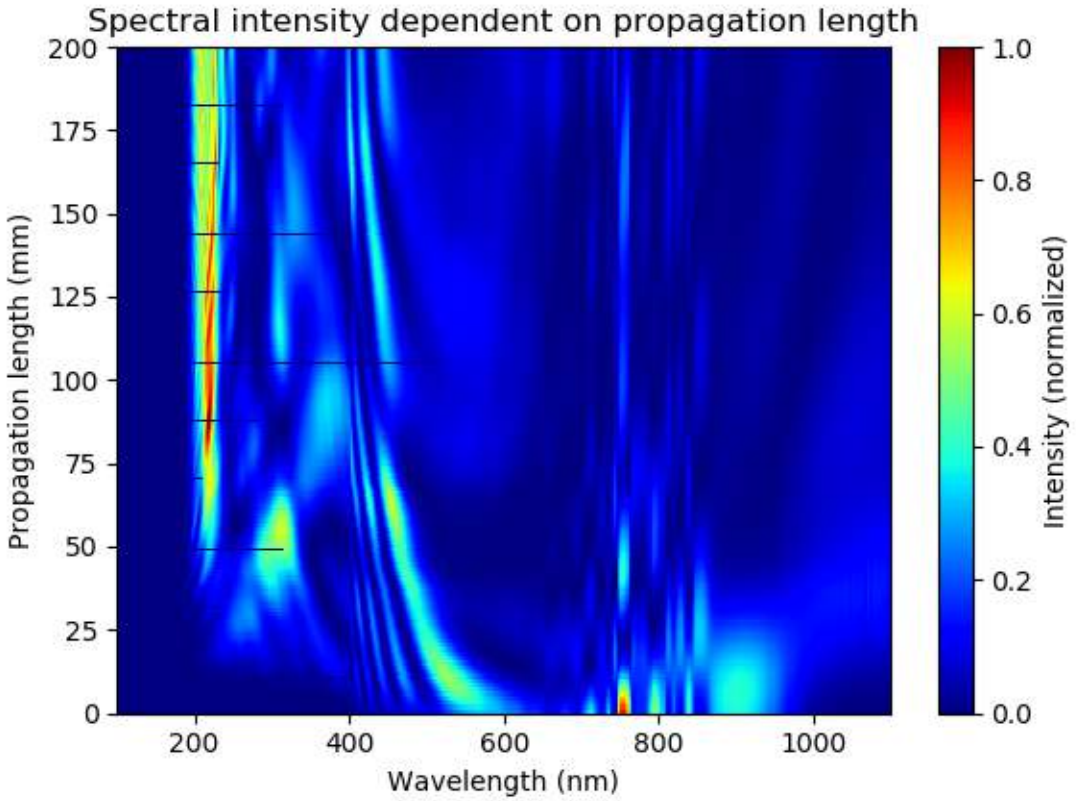

Figure 4.5: Spectral intensity simulated for $p = 1$ mbar argon in a fiber of $l = 200$ mm with an incident pulse energy of $E_{\mathrm{Pulse}} = 50\ \mu\mathrm{J}$. The generation of spectral components around 200 nm increases strongly at approximately 5 cm propagation length.

4.5 Discussion

The measurements in Figs. 4.1 and 4.2 show different characteristics. Fig. 4.1 shows a prominent peak in the UV for the different pressures with only a low intensity of wavelengths above approximately 260 nm. The measurements in Fig. 4.2 do not exhibit the peak or at least not as prominently and the spectrum is continuous in the UV wavelength range. Furthermore, it is interesting to note that in the former case the spectral components in the UV were measured even at the very low pressure of 25 mbar. In contrast, the strong effects of SPM are generally only observed in systems with higher pressures. Altogether, this is reason to believe that the measured spectra in Fig. 4.1 might stem partly from the generation of a resonant dispersive wave (RDW) in the UV. The spectrum measured at $p = 25$ mbar also does not show any spectral intensity above 260 nm which would be typical for a RDW that typically shows a high intensity peak in the UV. RDWs are usually generated at the condition of a very short duration of the pump pulse that is given in our setup. On the other hand, RDWs are usually generated with HCFs significantly longer than the fiber used in this setup. The measurements in Figs. 4.1 and 4.2 were conducted in October and December, respectively. Different experimental conditions are an explanation as to why the two measurements differ and while the conditions for generating a RDW might have been fulfilled at the first measurement the change in the setup in between the measurements might have lead to the conditions for the generation of the RDW no longer being valid.
Furthermore, the generation of the UV is clearly shown in both measurements, once limited by the absorption cutoff in oxygen and once reaching wavelengths down to approximately 170 nm as was the goal at the beginning of the thesis. This was not the case at all times when the laser was used at this setup. This can be explained with the constant change of the setup and the automation of it in the AS4-beamline. The fixation of the perforated mirrors, and the focusing into the fiber, as well as the focusing after the recombination of the two beams were all changed during the course of the thesis. Furthermore, the mirrors in the periscope were changed multiple times. Moreover, an imperfection in the focusing into the fiber can damage the fiber and influence the results that can be realized. Additionally, the conditions of the laser changed in between consecutive uses of the laser at the setup and even more so during the whole course of this thesis. To use the setup as a reliable source for DUV pulses in the future, the stabilization and reproducibility of the experimental parameters have to be increased further.
The theory presented in this thesis predicted the generation of the UV as the nonlinear optical process of SPM. Another explanation for the generation of spectral components at approximately 240 nm could be the process of third harmonic generation. The central wavelength of the input spectrum is approximately 780 nm. The third harmonic of this wavelength is located in the DUV at approximately 240 nm. The acquired data shows that the spectral components in the DUV are, in fact, generated via SPM as the spectrum in the DUV is continuous. Additionally, there is no CEP-dependence of these components, which excludes the possibility that third harmonic generation contributes considerably to the spectrum there.

The measurements in Fig. 4.2 can be used to evaluate the conversion efficiency of the generation of the UV spectral components. Via fitting of the measured spectrum at 1 bar, it can be calculated that only approximately 5% of the total pulse energy is contained in the UV spectral region of $170-340$ nm. Together with a measured power of approximately 35 mW after the fiber, that corresponds to a pulse energy of 8.75 μJ, which indicates an energy content of 450 nJ in the DUV to VUV spectral region in each pulse. Increasing the conversion efficiency and the absolute pulse energy in the UV spectral region is an important feature for the experiments that are planned in the future with the setup and several approaches are presented in the following.
Firstly, one approach for increasing the energy conversion efficiency is shown in Fig. 4.3. It is shown that the conversion efficiency is strongly increased when using a higher pulse energy. Further pulse energy control in the experimental setup can for example be achieved with the use of a different beam-splitting technique. The currently used perforated mirrors could be replaced with beam splitters, leading to higher power in the interferometer arm passing the fiber. This approach is however somewhat limited by ionization of the gas atoms in the fiber, which strongly affects the pulses. Ionization is not taken into account in the simulations.
Another approach is shown in Fig. 4.4. Increasing the pressure of argon inside the fiber also leads to a higher conversion energy of the UV spectral range. This approach could be realized in the setup as well. A concern in this case is the preservation of the vacuum conditions when using higher pressures of argon as the gas exits the fiber into the vacuum chamber through the ends of the fiber. The pressure can therefore not become too high. In the current setup problems arise at a pressure of approximately 1.5 bar above which the turbomolecular pumps can not be operated continuously.
Finally, simulations of the propagation of the laser pulse through a 20 cm long fiber, that are presented in Fig. 4.5, show that the use of a longer fiber than the ones used in the experiments might be another approach to increase the energy conversion efficiency. It is shown that the generation of UV spectral components, especially in the region of approximately 200 nm, increases strongly for a propagation in a fiber longer than approximately 5 cm. Such fibers are currently not in use in our experiments but they could be manufactured for the use in the setup.

Chapter 5

Field sampling

This chapter presents the results of the electric field-resolved measurements of the pulses. Firstly, the results conducted with the technique of tunneling ionization with a perturbation for the time-domain observation of an electric field (TIPTOE) are shown and discussed. Secondly, the data acquired with nonlinear photoconductive sampling (NPS) is presented and analyzed. Finally, techniques are compared with the analysis of the conducted measurements.

5.1 Setup

Both techniques (TIPTOE and NPS) and the setup used for the measurements are described in more detail in chapter 3. For both techniques the beam passes an interferometric setup, where the beam path is split into two arms. After the recombination of the two beams the measurement is conducted by assessing a current signal induced by the ionization of a gas or solid state material in between two electrodes. The aim of the field sampling methods is the field-resolved measurement of the pulses generated in the fiber that show an ultrabroadband spectrum as was presented in chapter 4. Therefore, the fiber is positioned in one arm of the interferometer, while the beam passing the other arm of the interferometer is not altered in TIPTOE and rotated in the polarization by 90° when measuring with the NPS technique.
Additionally to the measured electric field traces, the spectral components of the pulses are calculated and analyzed.

5.2 Experimental results with TIPTOE

With TIPTOE the electric field trace of the pulse passing the short 2.5 cm fiber is measured. Similar setup and beam parameters to the second measurement of the spectrum shown in Fig. 4.2 were used. The pulse energy is 50 μJ. The sample used to measure the current consists of copper electrodes while the ionizing medium is air.

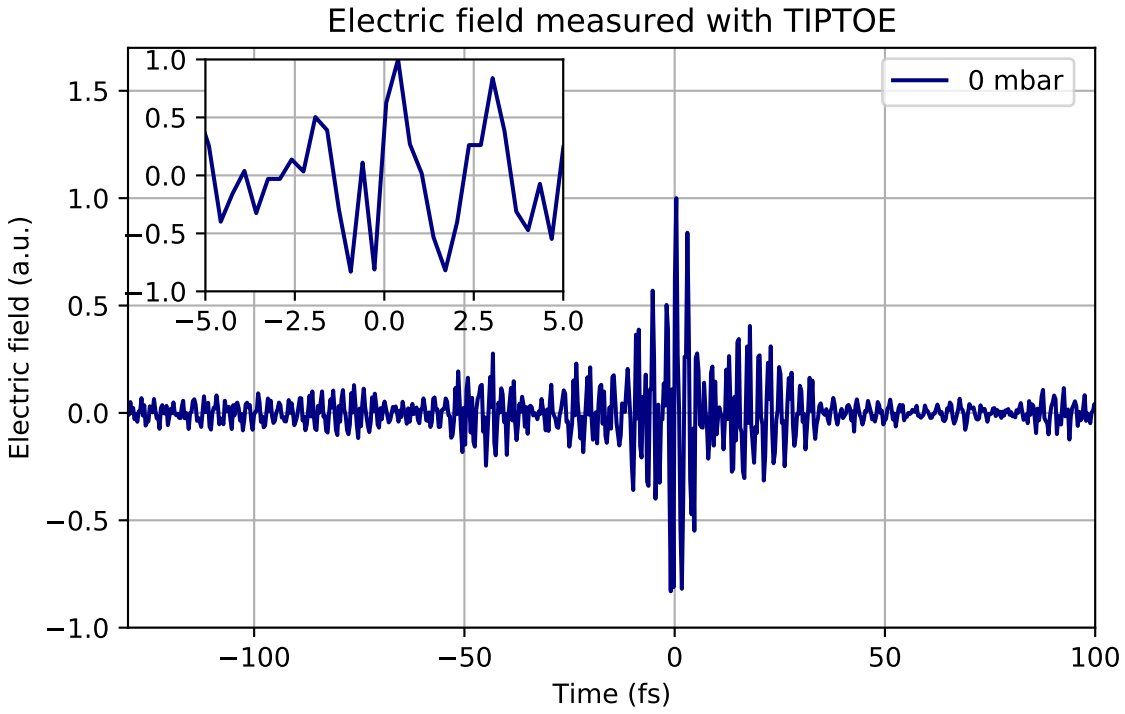

Figure 5.1: Electric field trace measured with TIPTOE with no gas in the fiber. The pulse is centered around $t = 0$ fs. The artifact is seen in the inset as the dips on top of the peaks.

Several traces for different pressures of argon in the fiber were recorded. The traces measured for $p = 0$ mbar and $p = 500$ mbar are shown in Figs. 5.1 and 5.2, respectively.
The change in the group velocity that the pulse experiences when passing the argon in the fiber leads to a delay of the pulse compared to a pulse that passes the fiber without gas in it. This delay can be calculated via the group velocity that is in turn the first derivative of the dispersion relation described in Eq. (3.6). For the short fiber and a pressure of 500 mbar, as measured here, the delay is calculated to be approximately 10 fs. Comparing the traces in Figs. 5.1 and 5.2, especially the secondary maxima, confirms the agreement of the measured delay with the theoretically calculated delay.
Furthermore, comparing the traces shows that the form of the pulse stays approximately the same. The shape and position of the secondary maxima stay approximately the same. The main maximum on the other hand looks as if it is expanded slightly in time. Additionally, there is no maximum peak at 10 fs as would be expected from the delay calculation. In contrast, there are two maxima at 0 fs and 20 fs.
Additionally, by using a windowed Fourier transform the temporal-spectral structure of the measured pulses can be analyzed. Here, the measured trace is multiplied by a Gaussian window with 10 fs (FWHM) for variable delays and then the Fourier transformation into

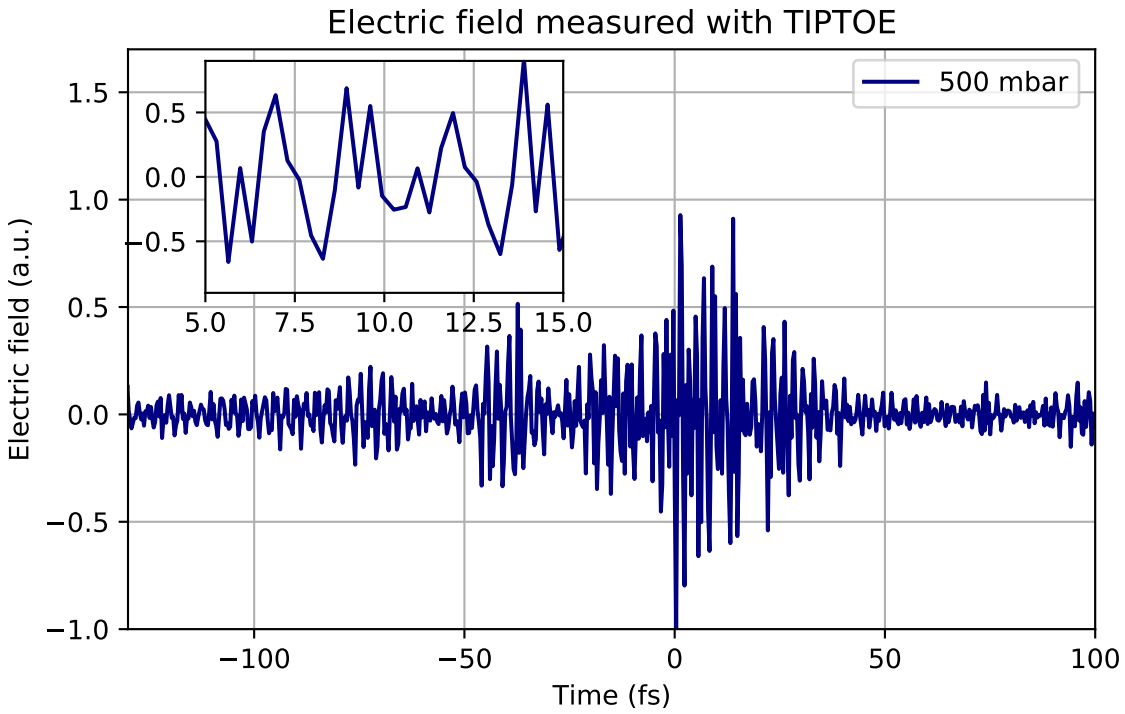

Figure 5.2: Electric field trace measured with TIPTOE for argon at $p = 500$ mbar in the fiber. Compared to the pulse with no argon in the fiber, the pulse is delayed approximately 10 fs. The artifact is clearly visible in the inset.

the spectral domain is performed for each delay. The colorplots showing the position of the different spectral components in the pulse are shown in Figs. 5.3 and 5.4 for no gas in the fiber and argon at $p = 500$ mbar, respectively. The spectral components between 0.2 PHz and 0.55 PHz correspond to the measured pulse. It can be seen that the presence of the gas in the fiber shifts the spectral components to higher frequencies.
Furthermore, there are spectral components in the range of 1 PHz and 1.1 PHz, respectively, in the region of the third harmonic of the pulse signal. These spectral components have a smaller intensity but they have a shape almost identical to the signal of the laser pulse, which is an indicator that they can be attributed to an artifact caused by the measurement setup (see also simulation below in Fig. 5.5).
Moreover, the artifact manifest in the temporal trace of the electric field, which is shown in the insets of Figs. 5.1 and 5.2. The peaks of the electric field traces mostly show a dip in the peak.
One explanation for this artifact could be the beam splitting method with the perforated mirrors. Despite being a common choice for the beam separation and recombination in literature [42, 38], potential problems might arise from the geometry of the focii. As the central part of the strong injection pulse that is reflected from the perforated mirror is missing, the focus of this beam shows a strong Airy-like pattern (see Fig. 3.4). Moreover, since the beam passing through the center of the perforated mirror has a larger focus size, the main maximum of the beam profile perpendicular to the propagation direction of this beam overlaps and interferes with both the main and the secondary maximum of the beam reflected from the perforated mirror as this beam is focused more tightly. The contribution arising from the secondary maximum is shifted in phase by π compared to the signal from the main maximum leading to a distortion of the measured signal. An approach to get rid of these distortions is the use of a different beam splitter and combiner.
A different reason that will need to be tested out is the potential spatial chirp of the beam. Since the injection pulse is missing the central part of the beam, the focus might be more strongly affected. Additionally, it needs to be further tested out if the ionization process is saturated which would lead to distortions in the recorded signal.
Consequently, the TIPTOE measurement technique as implemented in our setup is not suitable for measuring superbroadband continuum pulses reaching from the NIR to the UV before overcoming the limitation of the artifact in the UV spectral region. One approach would be to remove the NIR from the pulse and measure only the UV part of the pulse. As the artifact manifests in the region of the third harmonic, removing the NIR spectral component would potentially suppress the artifact or at least shift it to higher frequencies.

For comparison, the plot of the position of the spectral components is shown in Fig. 5.5 for the simulation data. The simulation was done for a fiber length of 6 cm at a pulse energy of 50 μJ and a pressure of 1000 mbar. The simulation parameters correspond to the parameters used in chapter 4. In contrast to the measured data, in the simulation data the high frequency components do not look like a copy of the original spectrum.

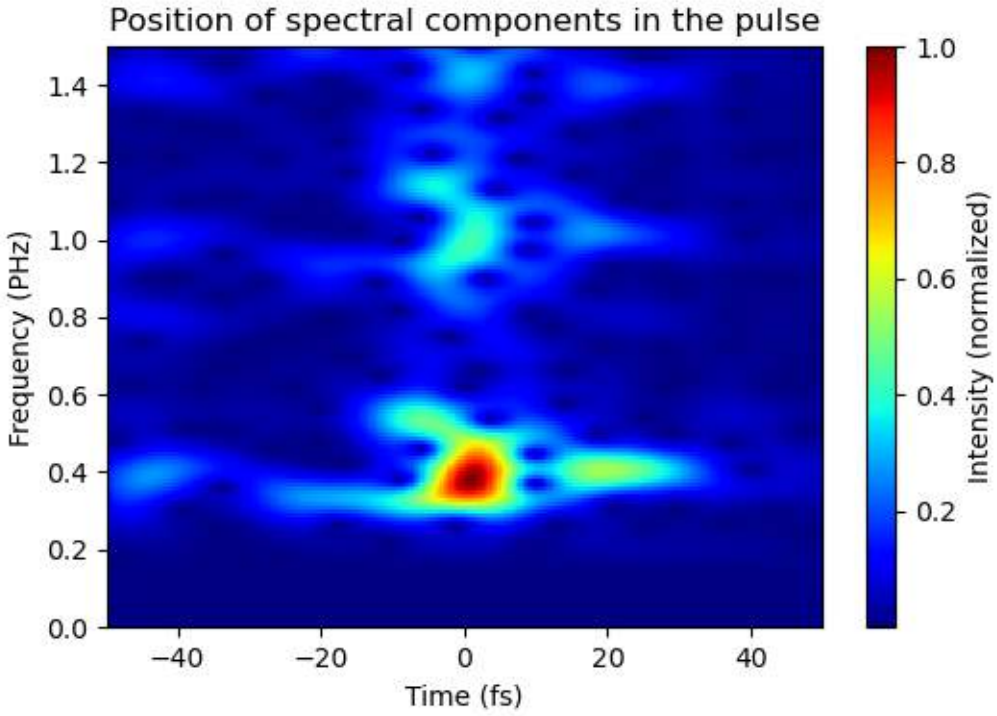

Figure 5.3: Colorplot of the position of the different frequency components in the pulse. This corresponds to the pulse shown in Fig. 5.1 with no gas in the fiber. The frequency components around 0.4 PHz correspond to the spectrum of the pulse. The frequency components around 1 PHz are an artifact steming from the measurement setup. This is indicated by the similar shape of the frequency components at 0.4 PHz and 1 PHz.

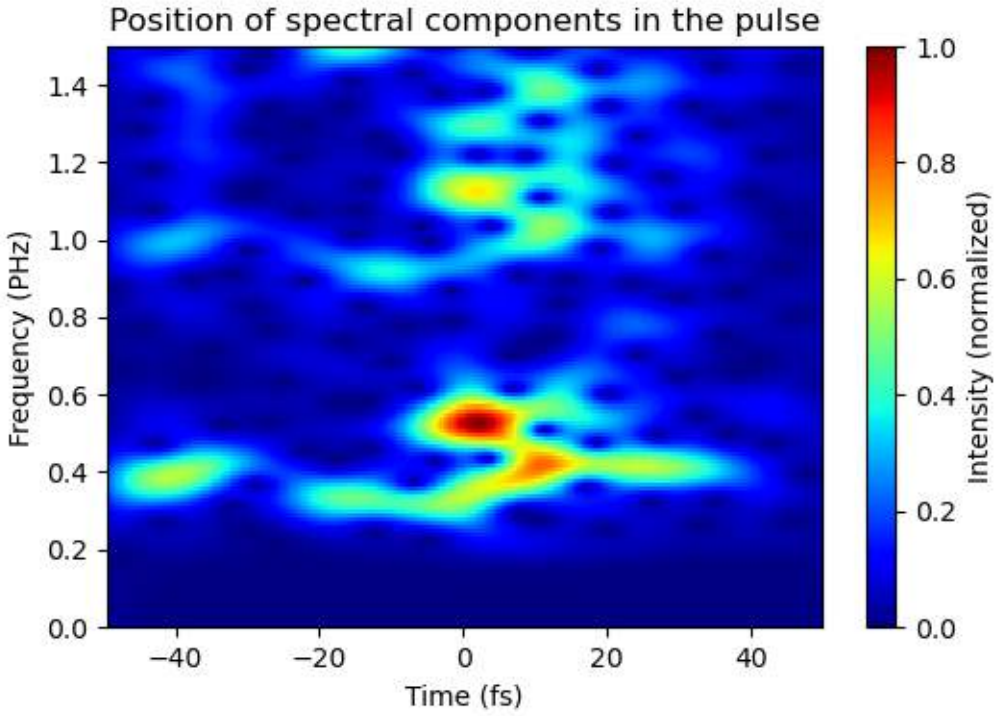

Figure 5.4: Colorplot of the position of the different frequency components in the pulse. This corresponds to the pulse shown in Fig. 5.2 with argon at a pressure of 500 mbar in the fiber. Compared to the measurement with no gas in the fiber shown in Fig. 5.3 the spectral components are shifted slightly to higher frequencies around 0.5 PHz. The artifact at around 1.1 PHz shows up in this measurement similarly to the measurement with no gas in the fiber.

The plot shows the position of the spectral components for a fiber length of 6 cm, shortly after the strong UV generation starts as was shown in chapter 4. The UV spectral components are located at the trailing edge of the incident laser pulse. They can therefore be associated to self-steepening which occurs there. It can be seen that the relative group delay of the spectral components in the region from 0.5 PHz to 1.5 PHz is smaller than 10 fs. This means that the pulses have a good compressibility as only a few chirped mirrors are needed to close the gap between the UV and VIS spectral components and therefore compress the pulse. This is only shown in the simulation data so far, but it indicates that there is a good chance of generating highly compressible pulses when using a longer fiber for the generation of the strong UV spectral components (see chapter 4).

In conclusion it can be said that while the technique of TIPTOE has the advantage to sample the electric field directly in theory, the UV spectral region we are interested in is at the moment dominated by an artifact. Finding the cause of the artifact and removing it should therefore be the top priority for advancing the TIPTOE measurements further. Fortunately the setup was designed such that it can easily be switched to allow NPS measurements by rotating the polarization of on interferometer arm. The results of the NPS measurements are described in the next section.

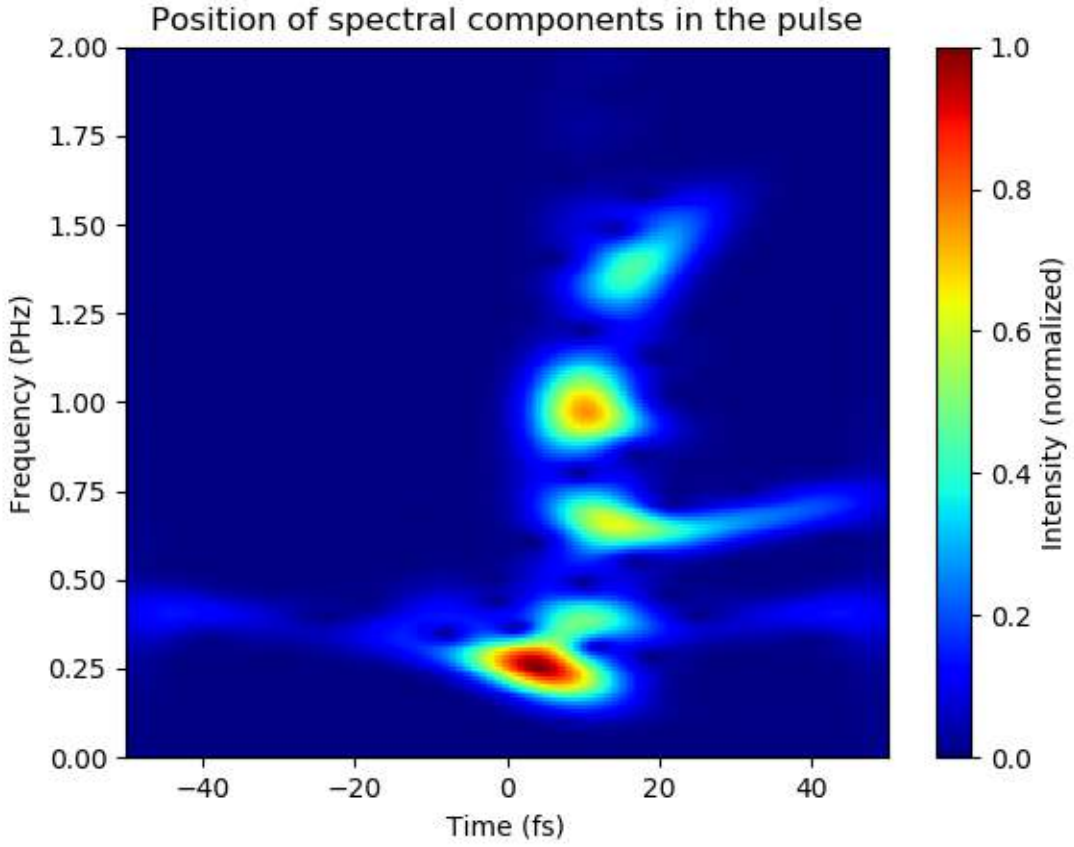

Figure 5.5: Colorplot of the position of the different frequency components in the pulse for a 6 cm long fiber at $p = 1000$ mbar argon and a pulse energy of 50 μJ simulated with pyNLO. The front of the pulse contains frequency components of around $0.3 - 0.4$PHz corresponding to the wavelength of the laser pulses. The higher frequency components generated by the nonlinear interactions in the argon-filled fiber are delayed.

5.3 Experimental results with NPS

Changing the polarization of one of the pulses, in the case of this setup, the polarization of the unchanged beam, enables the use of the NPS technique. The beam parameters are similar to the other measurements. A different sample of electrodes is used in this measurement compared to the TIPTOE technique. Here, the electrodes are made of gold and they are attached to a fused silica plate that serves as the ionizing medium. Similarly to the TIPTOE measurements the pulse passing the fiber is recorded with no gas and with different pressures of argon in the fiber. In contrast to the measurements conducted with TIPTOE, the long 5.5 cm fiber is used here. Fig. 5.6 shows the electric field traces recorded for 6 different sets of parameters where the pulse passes the fiber without gas and with argon at pressures from 200 mbar up to 1000 mbar in the fiber.
The delay of the pulse due to the change in the group velocity as described in section 5.2 is calculated for the mentioned parameters. The delay increases with the increase of the pressure in the fiber and at $p = 1000$ mbar the delay is approximately 55 fs. This is approximately the same delay as is measured and shown in Fig. 5.6.
Each of the traces shows the average of 5 single measurements. It is worth noting that the difference between these single measurements is non-negligible for some of the averaged traces for example for the traces recorded for 400 mbar. This is an indication that the setup is not completely stable. A reason for this could be the inaccuracy of the delay stage that changes the path length difference between the two interferometer arms due to the piezo stage operating in vacuum conditions. This would cause a distortion of the time axis and therefore fluctuations in the consecutive measurements.
Furthermore, the trace for $p = 1000$ mbar argon in the fiber is shown in Fig. 5.7 with a closer look at the trace from $t = 50$ fs up to $t = 55$ fs in the inset. The dips that were seen in the TIPTOE measurements do not show up here as prominently.

The spectrum of the measured pulses can be acquired by using a windowed Fourier transform of the electric field traces as described in section 5.2. The spectra for the pulses with no argon and argon at $p = 1000$ mbar are shown in Fig. 5.8. The peaks below the wavelength of approximately 300 nm are attributed to artifacts as they appear strongly for the pulse that passes the fiber without argon even though these pulses do not have spectral components in this wavelength region. Furthermore, if the pulse passes the fiber with argon, the spectrum is shifted towards smaller wavelengths. Additionally, new spectral components below approximately 400 nm appear that are generated from the nonlinear interaction of the pulse with the argon.
The wavelength region recorded in the measurements reaches mainly from 500 nm down to 300 nm. The lack of longer wavelengths that are present in the pulse as was shown in the recordings in chapter 4 is due to the fact that the response function, describing the strength of the response of the measurement technique to a particular frequency, has a minimum at the central frequency of the original pulse at approximately 0.4 PHz [2]. On the other hand, the response function shows a maximum at approximately 0.8 PHz corresponding to approximately 375 nm.

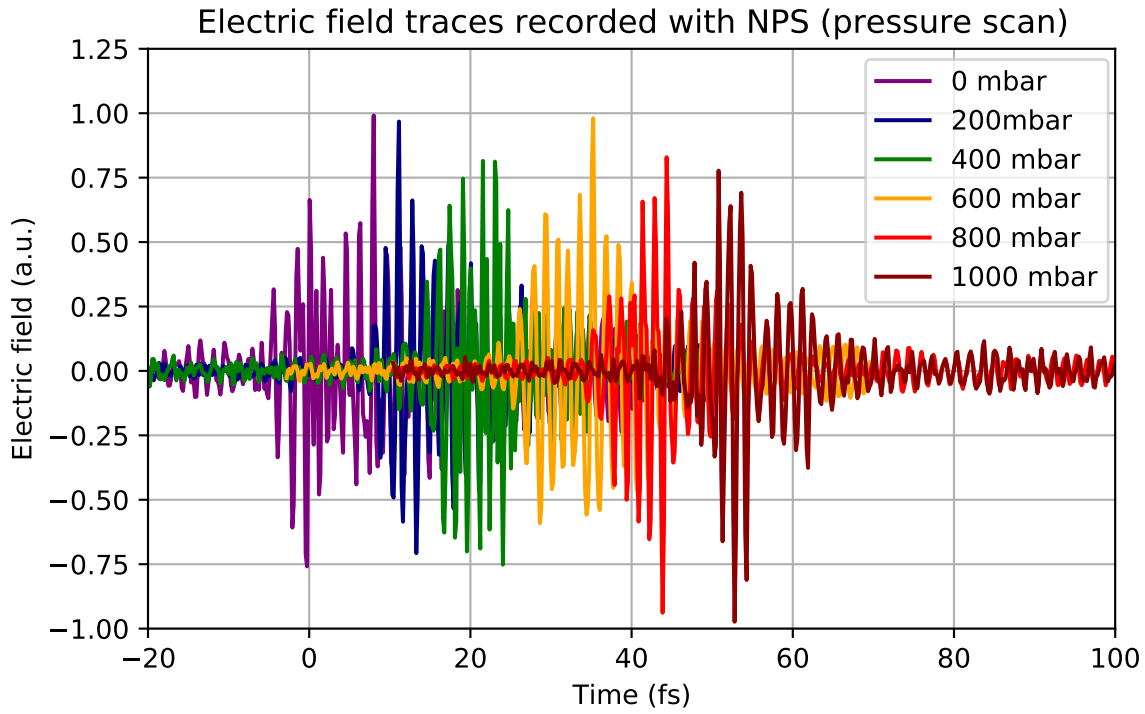

Figure 5.6: Electric field traces measured with the NPS technique. A pressure scan, varying the pressure in the fiber from $p = 0$ mbar (purple line) up to $p = 1000$ mbar (red line) is shown. The interaction of the pulses with the gas introduces a delay. Increasing the pressure leads to more interactions and a higher refractive index resulting in a longer delay. For $p = 1000$ mbar the pulse is delayed approximately 55 fs.

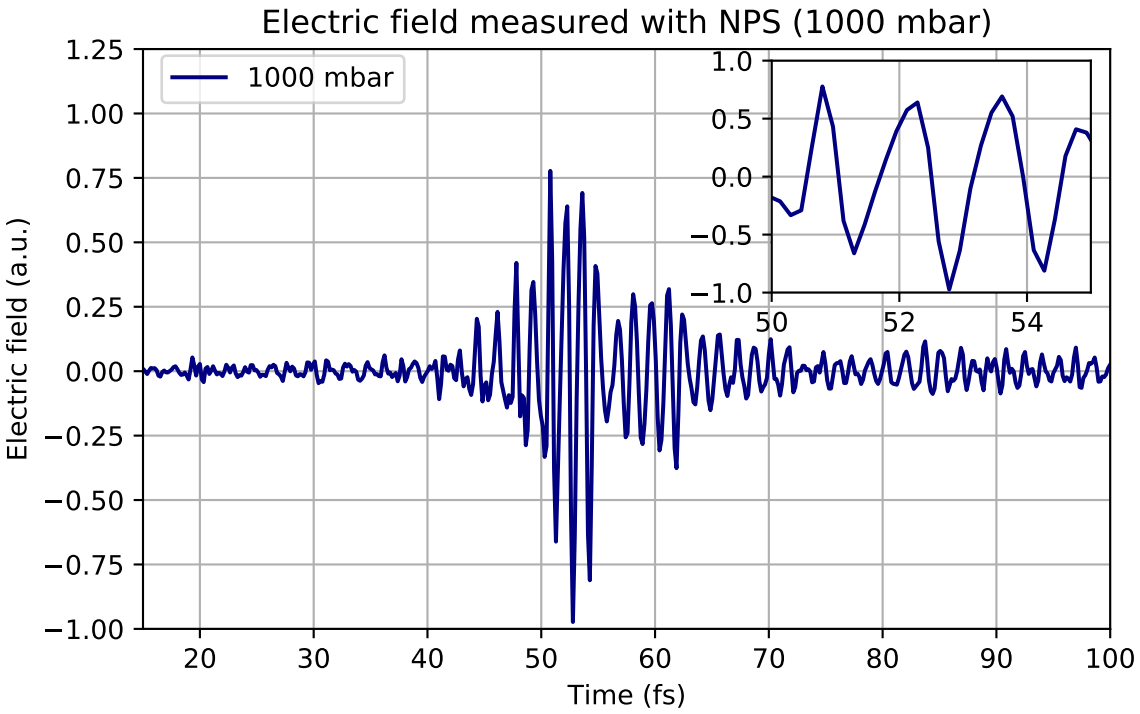

Figure 5.7: Electric field trace measured with NPS for argon at a pressure of $p = 1000$ mbar in the fiber. Dark red trace from Fig. 5.6. The inset shows the trace from $t = 50$ fs up to $t = 55$ fs. The delay compared to the pulse passing the fiber without the gas is approximately 55 fs.

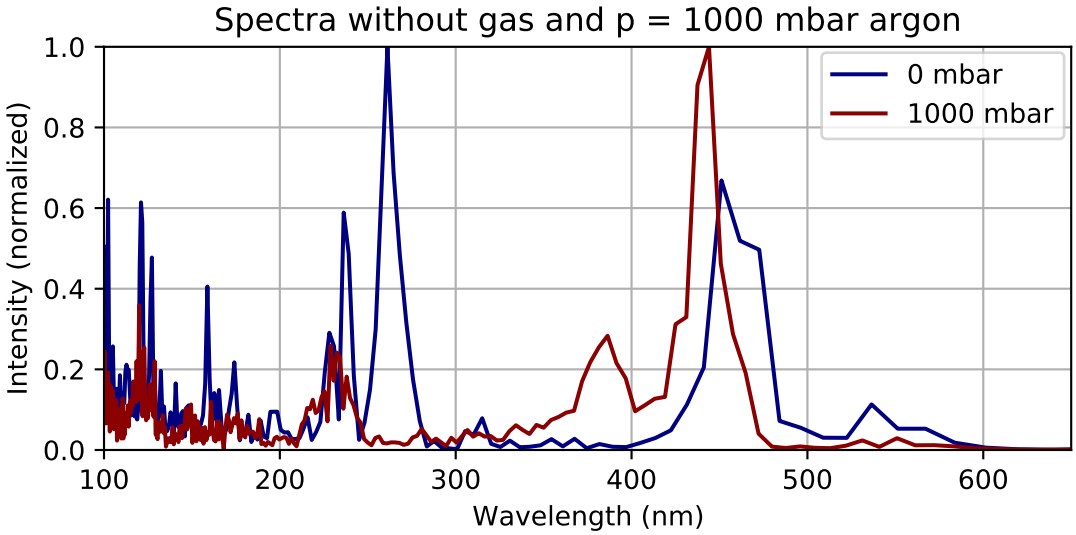

Figure 5.8: Spectra of the traces shown in Fig. 5.6 for $p = 0$ mbar (blue line) and $p = 1000$ mbar (red line) of argon. The peaks below $\lambda = 300$ nm are attributed to an artifact. The presence of the argon in the fiber shifts the spectrum towards the UV and creates spectral components below $\lambda = 400$ nm.

Fig. 5.9 shows the position of the spectral components in the pulse corresponding to a pressure of 1000 mbar in the fiber. Similarly to the TIPTOE measurements, the spectral components at approximately 1.3 PHz appear at the same position in the pulse as the spectral components at approximately 0.7 PHz corresponding to the incident pulse and show a similar shape. This is further confirmation that the small wavelength components are due to an artifact in the measurement.
Possible explanations for the appearance of this artifact are different focus spot sizes of the two beams, the spatial chirp of the beam, the saturation of the ionization and the instability of the interferometer, more precisely the delay stage. These possible explanations for the distortion and potential approaches to get rid of them are explained more closely in section 5.2.
Another approach for getting a better signal with the NPS method is the use of a different sample of electrodes and a different ionizing medium. Currently, measurements using argon as the ionizing medium are conducted.

Consequently, similar to TIPTOE, the NPS technique first has to overcome the limitations of generating artifacts in the wavelength region below 300 nm before being applicable as a measurement technique for pulses reaching down further in the wavelength range below 300 nm. Gaining more control over the beam parameters for both arms together and

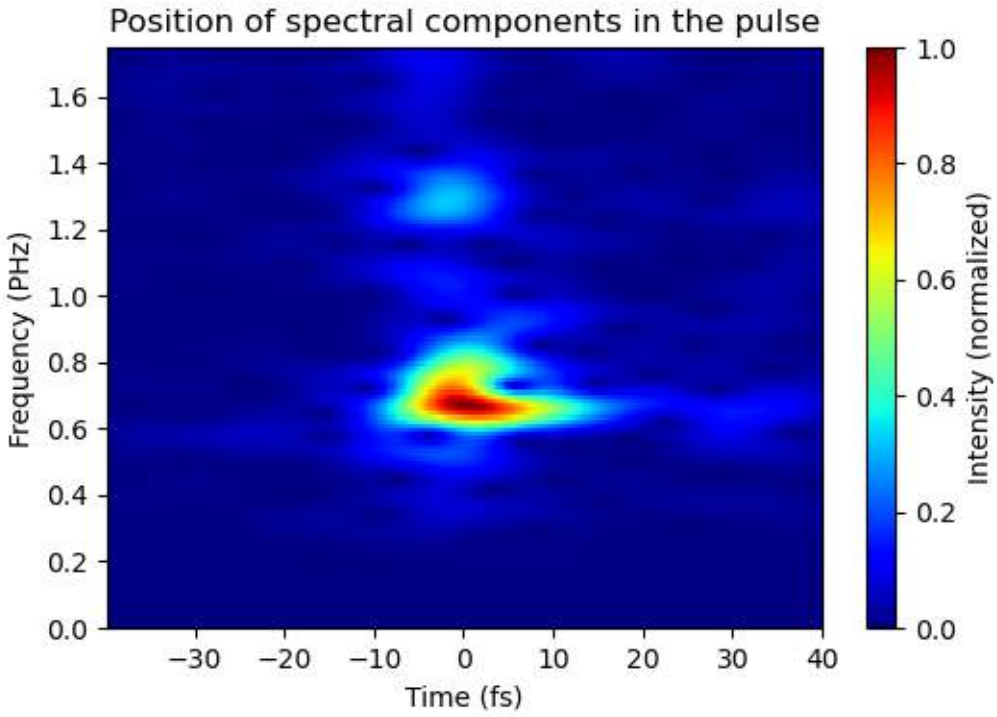

Figure 5.9: Colorplot of the position of the different frequency components in the pulse passing the fiber filled with $p = 1000$ mbar argon (NPS). The high frequency components at approximately 1.3 PHz appear at the same position in the pulse as the spectral components at approximately 0.65 PHz corresponding to the incident pulse. From simulation, they would be expected at the trailing edge of the pulse. Moreover, these spectral components are also present in the measurements of the unbroadened pulses (see Fig. 5.8). It can therefore be concluded that these high frequency components above 1 PHz can be attributed to an artifact.

individually, for example with more precise power and CEP control and different beam splitting and combining techniques is an approach to get rid of the artifacts and extend the measurement bandwidth in the setup. Moreover, the stability of the delay stage has to be ensured as unwanted movement could also be a source of the artifact.
Nevertheless, it should be mentioned that a shift of the pulses to the region of smaller wavelengths of approximately 400 nm can be observed with the technique. This region does not exhibit the artifact and can therefore be used for the characterization of the pulses.
The two methods shown in this (NPS) and the previous section (TIPTOE) are compared and discussed in the following section.

5.4 Comparison of TIPTOE and NPS

The two previous sections show the results obtained with the measurement techniques TIPTOE and NPS. Both techniques show the ability to record traces of the electric field that can in turn be used as a starting point for the spectral analysis of the pulse via Fourier transforming the electric field to get the spectral intensity.
In both techniques an artifact shows up in the UV spectral region making the techniques unsuitable for the measurement of superbroadband continuum pulses from the NIR to the UV. Different approaches to get rid of this artifact are the change of the beam splitting and combining methods as well as gaining improved control over the beam parameters. Exchanging the beam splitter would allow for an improved control of the power in the individual interferometer arms, which could improve the UV generation process. Furthermore, an improved control over the CEP and the dispersion in the individual arms could be realized with the usage of wedges and chirped mirrors in both arms. Additionally, the stability of the interferometer, especially of the delay stage, has to be established for further meaningful measurements. Another approach for now is to cut out the NIR spectrum of the measured pulse and only measure the UV spectral region. The goal is to extend both techniques from the NIR across the DUV region down to approximately 170 nm for the full characterization of the pulses generated via the nonlinear optical interactions in the argon-filled fiber.
Moreover, it is observed that the response functions, describing the strength of the response of the measurement setup to a particular frequency, of the two techniques highlight different wavelength regions depending on what technique is used. The maximum of the response function of TIPTOE is close to central frequency of the original pulse showing a high spectral intensity at approximately 0.4 PHz and a minimum of the measured signal at approximately 0.8 PHz, the second harmonic of the fundamental frequency. This is in contrast to the response function of the TIPTOE measurements, which has a maximum at the fundamental frequency [36]. The response function of NPS shows a minimum close to the central frequency of the original pulse and a maximum at approximately 0.8 PHz [2]. This allows to measure the shift of the wavelengths down to approximately $\lambda = 300$ nm caused by the nonlinear interaction of the pulse with the argon in the fiber.
Moreover, simulations of the position of the spectral components in the pulse after passing

a 6 cm long fiber showed the relative delay of the UV spectral region to be in the range of approximately 10 fs predicting a good compressibility of pulses generated in a longer fiber in the future.

Chapter 6

Conclusion and Outlook

This thesis describes the preparation of a high-vacuum experimental setup for the generation of DUV to VUV-pulses and their subsequent characterization via field-resolved measurement techniques. The setup is described in chapter 3.

In chapter 4 it was shown that pulses covering the whole DUV and extending down into the VUV to approximately $\lambda = 170$ nm were recorded during the course of this thesis. This proposes the use of these pulses for the investigation of ultrafast electron dynamics in small and large bandgap materials as it allows the linear excitation of these materials. The measured spectra leave room for further improvement in the area of reproducibility of the data on one hand and in the area of more efficient energy conversion on the other hand. Regarding the reproducibility, the stabilization of the parameters in the setup is the key component. For the increase of the conversion efficiency, the simulations offer a starting point. The increase of the pulse energy, the pressure of the argon in the fiber and the length of the used fiber all showed an increase in conversion efficiency. All of these approaches can be tested out experimentally in the future course of the project. The next step after reaching the ultrabroadband spectrum is the compression of these pulses down to their Fourier limited duration. Furthermore, experiments utilizing the high energetic photons and their application in the linear excitation of different materials are planned subsequently.

Additionally, in chapter 5 electric-field resolved measurements were conducted with the techniques TIPTOE and NPS. The analysis of the spectrum corresponding to the measured pulses showed artifacts in the wavelength region below 300 nm for both measurement techniques making it impossible to measure in this wavelength region. This region is particularly interesting for the characterization of the pulses passing the argon-filled fiber with a spectrum extending down to approximately 170 nm. Nevertheless, the NPS technique showed the extension of the spectrum when passing the argon-filled fiber down to approximately 300 nm. Compared to TIPTOE this is possible due to the different positions of the maxima of the response functions. The next step regarding both field sampling techniques is to extend the lower wavelength limit by getting rid of the artifact. The approaches discussed in chapter 5 include the change of the beam splitting and combining technique,

gaining more control over the beam parameters of the individual interferometer arms and stabilizing the interferometric setup in general. Furthermore, the use of different materials for the ionizing medium and the electrodes is an approach to extend the bandwidth of the techniques.

In conclusion, the work described in this thesis lays the foundation for reaching the goal of the generation and field-resolved characterization of ultrabroadband continua from the DUV to NIR region.

Appendix A

Data archiving

The experimental raw data, the python files for evaluating the data, the python code used for the simulations (modified pyNLO) and all figures in this thesis are archived on the server of the Laboratory for Attosecond Physics at the Max Planck Institute of Quantum Optics:

`/afs/ipp-garching.mpg.de/mpq/lap/publication_archive/new_publications/`

The readme files in the folder explain the organization of the data, the use of the evaluation codes and the use of the simulation code.

Bibliography

[1] Seung Beom Park, Kyungseung Kim, Wosik Cho, Sung In Hwang, Igor Ivanov, Chang Hee Nam, and Kyung Taec Kim. Direct sampling of a light wave in air. *Optica*, 5(4):402–408, April 2018.

[2] Shawn Sederberg, Dmitry Zimin, Sabine Keiber, Florian Siegrist, Michael Wismer, Vladislav S. Yakovlev, Isabella Floss, Christoph Lemell, Joachim Burgdörfer, Martin Schultze, Ferenc Krausz, and Nicholas Karpowicz. Attosecond optoelectronic field measurement in solids. *Nature Communications*, 11, January 2020.

[3] T. H. Maiman. Stimulated optical radiation in ruby. *Nature*, 187:493–494, 1960.

[4] Fred J. McClung and Robert W. Hellwarth. Giant optical pulsations from ruby. *Journal of Applied Physics*, 33:828–829, 1962.

[5] Hans W. Mocker and Robert J. Collins. Mode competition and self-locking effects in a q-switched ruby laser. *Applied Physics Letters*, 7:270–273, 1965.

[6] P. F. Moulton. Spectroscopic and laser characteristics of Ti:Al2O3. *Journal of the Optical Society of America B.*, 3(1):125–133, January 1986.

[7] Marcos Dantus, Mark J. Rosker, and Ahmed H. Zewail. Real-time femtosecond probing of "transition states" in chemical reactions. *The Journal of Chemical Physics*, 87(4):2395–2397, 1987.

[8] Karl W. Böer. *Bands and Band Gaps in Solids*, pages 105–147. Springer Berlin Heidelberg, Berlin, Heidelberg, 2013.

[9] Jean-Claude Diels and Wolfgang Rudolph. *Ultrashort Laser Pulse Phenomena*. Academic Press, 2nd edition, 2006.

[10] Rick Trebino and Erik Zeek. *Ultrashort Laser Pulses*, pages 11–35. Springer US, Boston, MA, 2000.

[11] Robert W. Boyd. *Nonlinear Optics*. Academic Press, 3rd edition, 2008.

[12] A. Couairon and A. Mysyrowicz. Femtosecond filamentation in transparent media. *Physics Reports*, 441(2):47–189, 2007.

[13] Leonid Veniaminovich Keldysh. Ionization in the field of a strong electromagnetic wave. 1964.

[14] A. Perelomov, V. Popov, and M. Terent'ev. Ionization of Atoms in an Alternating Electric Field. *Soviet Journal of Experimental and Theoretical Physics*, 23:924–934, November 1966.

[15] A. Perelomov, V. Popov, and M. Terent'ev. Ionization of Atoms in an Alternating Electric Field: II. *Soviet Journal of Experimental and Theoretical Physics*, 24:207–217, January 1967.

[16] Johannes Schötz. *Field-resolved studies of ultrafastlight-matter interaction*. PhD thesis, Ludwig-Maximilians-Universität München, 2021.

[17] J. H. Eberly and J. Javanainen. Above-threshold ionisation. *European Journal of Physics*, 9(4):265–275, October 1988.

[18] H. G. Muller, Adriaan Tip, and Marnix van der Wiel. Ponderomotive force and AC Stark shift in multiphoton ionisation. *Journal of Physics B*, 16, 1983.

[19] Maxim V. Ammosov, Nikolai B. Delone, and Vladimir P. Krainov. Tunnel Ionization Of Complex Atoms And Atomic Ions In Electromagnetic Field. In John A. Alcock, editor, *High Intensity Laser Processes*, volume 0664, pages 138 – 141. International Society for Optics and Photonics, SPIE, 1986.

[20] P. B. Corkum. Plasma perspective on strong field multiphoton ionization. *Phys. Rev. Lett.*, 71:1994–1997, Sep 1993.

[21] G. G. Paulus, W. Becker, W. Nicklich, and H. Walther. Rescattering effects in above-threshold ionization: a classical model. *Journal of Physics B: Atomic, Molecular and Optical Physics*, 27(21):L703–L708, November 1994.

[22] Carsten Winterfeldt, Christian Spielmann, and Gustav Gerber. Colloquium: Optimal control of high-harmonic generation. *Rev. Mod. Phys.*, 80:117–140, January 2008.

[23] Thorsten Uphues. Course 2: Basic Technologies - Part III: High Harmonic Generation - The route to sub-fs physics. URL: `https://ufox.cfel.de/sites/sites_cfelgroups/site_cfel-ufox/content/e16281/e86791/e86828/e86829/e86834/2013_04_18UFSC_Lec_4.pdf` (Visited on 17/03/2022), 2013.

[24] Elisabeth Monika Ludmilla Bothschafter. *Femtosecond and Attosecond Electron Dynamics in Semiconductors and Dielectrics*. PhD thesis, Technische Universität München, 2013.

[25] Florian Andreas Siegrist. *Light-Field Driven Chargeand Spin Transfer*. PhD thesis, Ludwig-Maximilians-Universität München, 2019.

[26] Donna Strickland and Gerard Mourou. Compression of amplified chirped optical pulses. *Optics Communications*, 56(3):219–221, 1985.

[27] White paper: Principles of lock-in detection. Technical report, Zurich Instruments, 2016.

[28] Amelie Schulte, Corinna Konrad, Julia Anthea Gessner, Matthew Weidman, Vladislav Yakovlev, Johannes Schötz, and Ferenc Krausz. Towards Field Sampling of Ultrabroadband Continuum Radiation from deep-UV to NIR. 2021.

[29] pyNLO: Nonlinear optics modeling for Python, 2022.

[30] Johan Hult. A fourth-order runge–kutta in the interaction picture method for simulating supercontinuum generation in optical fibers. *Journal of Lightwave Technology*, 25(12):3770–3775, 2007.

[31] C. Vozzi, M. Nisoli, G. Sansone, S. Stagira, and S. De Silvestri. Optimal spectral broadening in hollow-fiber compressor systems. *Applied Physics B*, 80:285–289, 2005.

[32] John C. Travers, Teodora F. Grigorova, Christian Brahms, and Federico Belli. High-energy pulse self-compression and ultraviolet generation through soliton dynamics in hollow capillary fibres. *Nature Photonics*, 13:547–554, 2019.

[33] Carsten Bree, Ayhan Demircan, and Günter Steinmeyer. Method for computing the nonlinear refractive index via keldysh theory. *IEEE Journal of Quantum Electronics*, 46(4):433–437, 2010.

[34] A. Börzsönyi, Z. Heiner, M. P. Kalashnikov, A. P. Kovács, and K. Osvay. Dispersion measurement of inert gases and gas mixtures at 800 nm. *Appl. Opt.*, 47(27):4856–4863, September 2008.

[35] Michael Heynck. A systematic study of multi-octave spectral broadening in a hollow core capillary. Master's thesis, Ludwig-Maximilians-Universität München, 2021.

[36] Mina R. Bionta, Felix Ritzkowsky, Marco Turchetti, Yujia Yang, Dario Cattozzo Mor, William P. Putnam, Franz X. Kärtner, Karl K. Berggren, and Phillip D. Keathley. On-chip sampling of optical fields with attosecond resolution. *Nature Photonics*, 2021.

[37] Sung In Hwang, Seung Beom Park, Jehoi Mun, Wosik Cho, Chang Hee Nam, and Kyung Taec Kim. Generation of a single-cycle pulse using a two-stage compressor and its temporal characterization using a tunnelling ionization method. *Scientific Reports*, 2019.

[38] Wosik Cho, Sung In Hwang, Chang Hee Nam, Mina R. Bionta, Philippe Lassonde, Bruno E. Schmidt, Heide Ibrahim, François Légaré, and Kyung Taec Kim. Temporal characterization of femtosecond laser pulses using tunneling ionization in the uv, visible, and mid-ir ranges. *Scientific Reports*, 2019.

[39] Agustin Schiffrin, Tim Paasch-Colberg, Nicholas Karpowicz, Vadym Apalkov, Daniel Gerster, Sascha Mühlbrandt, Michael Korbman, Joachim Reichert, Martin Schultze, Simon Holzner, Johannes V. Barth, Reinhard Kienberger, Ralph Ernstorfer, Vladislav S. Yakovlev, Mark I. Stockman, and Ferenc Krausz. Optical-field-induced current in dielectrics. *Nature*, 493, 2013.

[40] Dmitry Zimin, Matthew Weidman, Johannes Schötz, Matthias F. Kling, Vladislav S. Yakovlev, Ferenc Krausz, and Nicholas Karpowicz. Petahertz-scale nonlinear photoconductive sampling in air. *Optica*, 8(5):586–590, May 2021.

[41] Guy P. Brasseur and Susan Solomon. *Radiation*, pages 151–264. Springer Netherlands, Dordrecht, 2005.

[42] Nariyuki Saito, Nobuhisa Ishii, Teruto Kanai, and Jiro Itatani. All-optical characterization of the two-dimensional waveform and the gouy phase of an infrared pulse based on plasma fluorescence of gas. *Opt. Express*, 26(19):24591–24601, Sep 2018.

Acknowledgements

Firstly, I want to thank Professor Ferenc Krausz for the possibility to write my master thesis in the attosecond physics group and working with an advanced laser system.

Secondly, I am very thankful to my supervisor, Dr. Johannes Schötz, for all his support in writing the thesis by always being a helpful contact person in the lab, while writing the thesis and in general.

Additionally, I want to thank Dr. Matthew Weidman for introducing me into the realm of ultrafast physics.

Furthermore, I would like to thank Amelie Schulte for showing me the handling and maintaining of the laser system and spending countless hours in the lab with me recording data for the thesis.

Also, I would like to thank all members of the attosecond metrology 2.0 team for the constructive discussions and the educational time that I could spend in the group.

Lastly, I want to thank my family and friends for reading my thesis and helping me improve it even though the topic was not in their area of expertise.

Eidesstattliche Erklärung

Hiermit erkläre ich, die vorliegende Arbeit selbstständig verfasst zu haben und keine anderen als die in der Arbeit angegebenen Quellen und Hilfsmittel benutzt zu haben.

München, den 23. März 2022

Corinna Melanie Konrad